INNOVATION FOREVER
Open Access

Innovation Discovery
ISSN 2959-5150 (Online)

Research Article

Effect of Temperature on Dielectric Properties of $Ni_{1-2x}Mg_xRu_xO$ Nanoparticles and Nyquist Plot Analysis

Alexandra Alkhatib[1], Zouheir Bitar[1*]

[1]*Physics Department, Beirut Arab University, Beirut, Lebanon*

[*]***Correspondence to: Zouheir Bitar, PhD, Assistant Professor,*** *Physics Department, Beirut Arab University, Tarik El Jadida, P.O.Box 11-5020, Riad El Solh 1107 2809, Beirut, Lebanon; Email: zouheirbitar@hotmail.com*

Abstract

$Ni_{1-2x}Mg_xRu_xO$ nanoparticles (x=0, 0.005, 0.01, 0.04, 0.08) were synthesized using EDTA as a capping agent and salt chloride as a precursor, employing the chemical co-precipitation technique. The X-ray diffractometer results confirmed the successful formation and crystallisation of $Ni_{1-2x}Mg_xRu_xO$ nanoparticles with an fcc structure and confirmed the formation of a secondary phase, RuO_2, for x=0.04 and 0.08. The dielectric properties of both samples exhibit a significant temperature dependence. AC conductivity and dielectric constant increased with temperature but peaked at 210°C for $Ni_{1-2x}Mg_xRu_xO$, followed by a drop. In contrast, the impedance decreased with increasing temperature; however, this decrease exhibited nonlinear behaviour in the co-doped samples. Nyquist plot analysis showed different equivalent circuits for different concentrations of dopants, which confirms the effect of dopants on the NiO.

Keywords: co-precipitation, dielectric properties, Nyquist plot, NiO

Received: August 19, 2025
Revised: May 6, 2026
Accepted: June 3, 2026
Published: June 16, 2026

Copyright © 2026 The Author(s). Published by Innovation Forever Publishing Group Limited. This open-access article is licensed under a Creative Commons Attribution 4.0 International License (https://creativecommons.org/licenses/by/4.0), which permits unrestricted use, sharing, adaptation, distribution, and reproduction in any medium, provided the original work is properly cited.

Citation: Alkhatib A, Bitar Z. Effect of Temperature on Dielectric Properties of $Ni_{1-2x}Mg_xRu_xO$ Nanoparticles and Nyquist Plot Analysis. *Innov Discov*, 2026; 3(2): 9.

1 INTRODUCTION

Over the past twenty-two years, nickel oxide (NiO) has been extensively investigated for use in catalysis, energy storage, and electronics[1]. This p-type semiconductor combines good chemical stability with tunable electronic properties, offering a suitable platform for the future development of advanced functional materials, especially nanostructured NiO, which has enhanced surface area and quantum confinement effects, thus increasing prospects[2]. To modulate such electrical properties tailored for specific applications, different doping strategies have been studied. While many researchers have begun investigating doped nanomaterials, research on Mg-doped NiO nanoparticles remains limited, with most studies focusing on structural, magnetic, and optical properties such as crystallinity, bandgap energy, and magnetic ordering[3]. Doping some foreign ions into the NiO lattice effectively changes its charge carrier concentration, the chemistry of defects, and, finally, its dielectric response[4]. However, similar to Mg-doped NiO, not one of the studies on Ru-doped NiO nanoparticles examined dielectric properties[5,6]. Among the various dopants, Mg and Ru have appeared promising in modifying the properties of metal oxides. Mg substitutes into the NiO lattice, as its ionic radius is comparable to that of Ni, and forms acceptor defects that influence the material's conductivity[7]. Ru, a transition metal, introduces extra electronic states and can also contribute to mixed valence effects that promote diverse electronic behavior of the material[6]. To date, there has also been no work using NiO nanoparticles doped with Mg and Ru concurrently that investigates their effect on the dielectric properties of the material, nor is there any work that examined both dopants in this combination with other nanoparticles[8]. In most of the dual-doped NiO systems reported in the literature, none examined dielectric properties, and of those that did examine

dielectric properties, only a limited number examined the dielectric response as a function of temperature and dopant concentration[4]. Co-doping with Mg and Ru provides a synergistic mechanism for fine-tuning the dielectric properties of NiO nanoparticles to develop new materials for enhanced dielectric performance[8]. It is thus imperative to deepen understanding of the dielectric properties of dual-doped NiO nanoparticles for optimizing performance in applications such as capacitors, sensors, and microwave devices. Dielectric spectroscopy, which enables the assessment of the electrical response of materials in varied frequency fields, allows for a richer insight into the mechanisms associated with polarization and relaxation processes within the material[9]. Inspired by these gaps in the literature, this study explores for the first time the dielectric properties of $Ni_{1-2x}Mg_xRu_xO$ (x=0, 0.005, 0.01, 0.04, 0.08) nanoparticles synthesized by the co-precipitation method in the frequency range (0.1-8MHz) and with varying temperature from 30 to 240°C.

2 MATERIALS AND METHODS

2.1 Preparation Method

Among the several methods for synthesizing nanoparticles, the co-precipitation method was selected to produce pure NiO and $Ni_{1-2x}Mg_xM_xO$ nanoparticles where M=Ru and x=0.005, 0.01, 0.04, 0.08. Pure NiO and $Ni_{1-2x}Mg_xRu_xO$ were produced at a reaction temperature of 60°C. Initially, the wet chemical synthesis phase was initiated, in which a 1 M salt chloride precursor was weighed based on the desired elemental composition of the pure or co-doped final product, using stoichiometric calculations. Following this, corresponding stoichiometric amounts were dissolved using deionized water. The synthesized solutions were then combined and added to 0.1 M EDTA, which serves as a capping agent to control the size of the nanoparticles and reduce agglomerations. Based on the quantities used, the molar ratio of EDTA to total metal cations was approximately 0.13:1 (0.0134mol EDTA to ~0.10mol total metal ions). The green solutions were then titrated by adding 4M NaOH dropwise while stirring continuously after being magnetically agitated for 30 minutes. The titration was stopped when the pH reached 13, and the obtained solutions were magnetically stirred for two hours at 60°C. After that, the resulting green items were consistently rinsed with deionized water until the pH of the filtered water dropped to 7. Precipitates were dried at 100°C for 20 hours, then manually crushed into fine powders and calcined at 550°C for 4 hours to achieve the crystalline structure and desirable morphology. Thermogravimetric analysis (TGA) was used to determine the calcination temperature. The calcination temperature of 550°C is justified by TGA in Figure S1 in the electronic supplementary information (ESI).

2.2 Characterization

The synthesized NiO nanoparticles were co-doped with Mg and Ru, and their structural and dielectric properties were evaluated. The X-ray powder diffraction (XRD) analysis was carried out using the D8 Focus (Bruker Co., USA). Rietveld refinement was performed via the Materials Analysis Using Diffraction (MAUD) software to ensure phase formation and purity. Conversely, the dielectric characteristics of pure NiO and $Ni_{1-2x}Mg_xRu_xO$ (x=0.005, 0.01, 0.04, 0.08) nanoparticles were examined using an impedance analyzer (Hioki, IM7581). The temperature and frequency-dependent dielectric performance and the impact of co-doping on the charge transport and relaxation mechanisms of the nanoparticles were examined using impedance spectroscopy. Every sample was tested using a frequency range of (0.1-8MHz) and an increasing temperature from 30 to 240°C via an electrical oven.

3 RESULTS AND DISCUSSION

3.1 XRD Analysis

Figure 1 shows that the XRD patterns of all the synthesized nanoparticles confirm that the $Ni_{1-2x}Mg_xRu_xO$ nanoparticles and their crystallization in the fcc structure of space group Fm3m, indexed by (111), (200), (220), (311), and (222) planes, were successfully prepared. Pure and (Mg, Ru) co-doped NiO nanoparticles show five major diffraction peaks in the XRD spectra. For the refinement of the Rietveld, XRD patterns were fitted using MAUD software[10]. The synthesized nanoparticles confirm a secondary RuO_2 phase, which is revealed for the $Ni_{0.92}Mg_{0.04}Ru_{0.04}O$ and $Ni_{0.84}Mg_{0.08}Ru_{0.08}O$ nanoparticles. The formation of RuO_2 indicates that Ru can dissolve into the NiO lattice to a limit of x=0.01, after which it can no longer merge into the NiO lattice; consequently, it begins to segregate at grain boundaries and forms a secondary phase of 1.73% and 7.89% for x=0.04 and x=0.08, respectively. The absence of organic residues and the preservation of the NiO lattice upon doping are confirmed by the Fourier Transform Infrared Spectroscopy in Figure S2 in the ESI. The homogeneous nanoparticle morphology and the incorporation of Mg and Ru (with Ru detected only for x≥0.04) are demonstrated by SEM (Scanning Electronic Microscope)-EDX (Energy Dispersive X-ray) in Figure S3 and Table S1 in the ESI.

3.2 Dielectric Constant vs Temperature and Frequency

Figure 2B-E shows a significant increase in real (ε′) and imaginary (ε′′) parts of the dielectric constant for $Ni_{1-2x}Mg_xRu_xO$ nanoparticles as temperature increases from 30 to 210°C at selected frequencies (0.2, 0.3, 0.5, 1, 2.5, 5, 7.5MHz) and for all dopant concentrations (0.005, 0.01, 0.04, 0.08). A notable peak is detected at 210°C, followed by a drop upon reaching 240°C. The dielectric parameter is complex due to the application of an alternating electric field to a capacitor containing a dielectric material, pure NiO, and $Ni_{1-2x}Mg_xRu_xO$

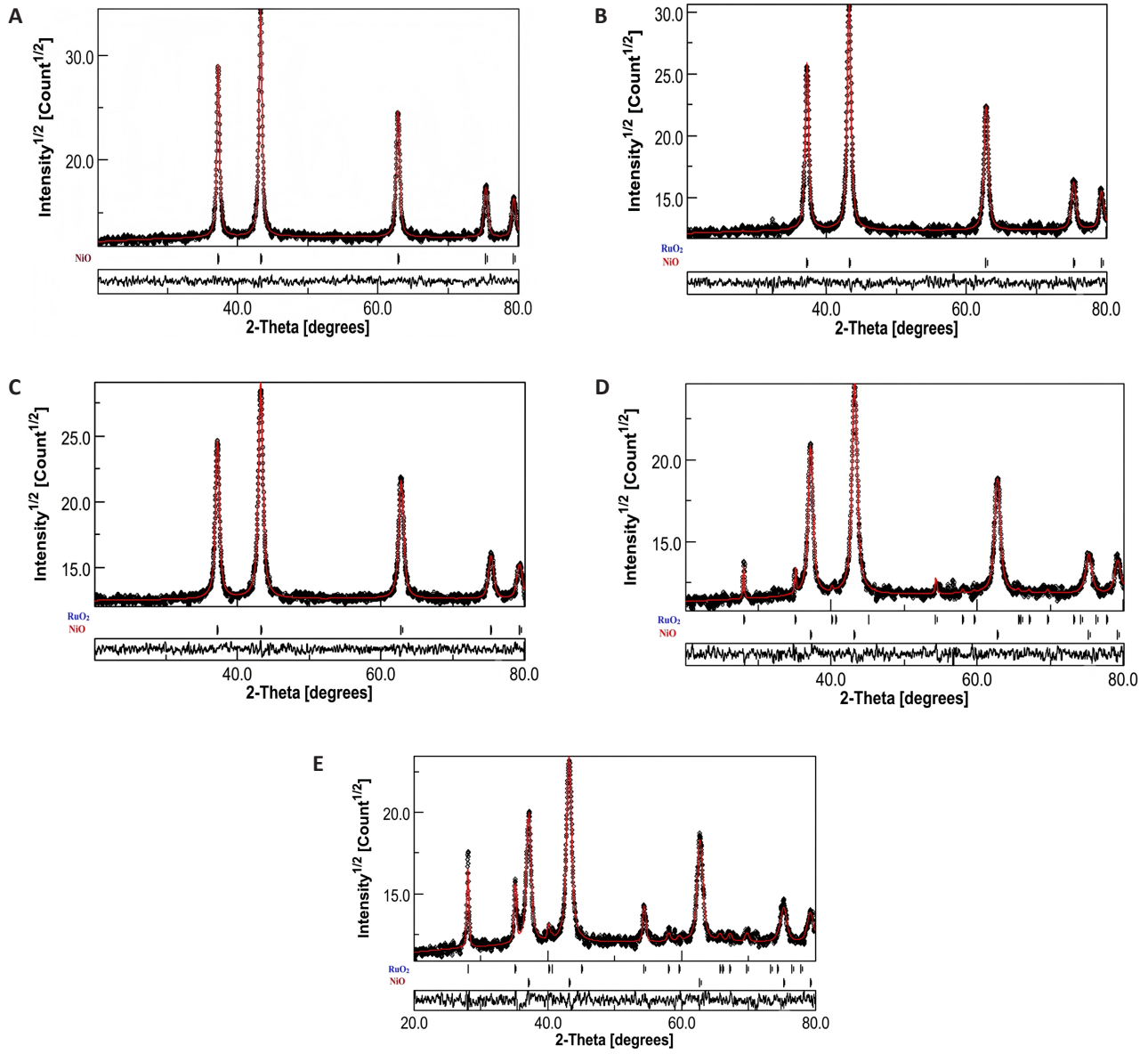


Figure 1. Refined XRD Patterns of $Ni_{1-2x}Mg_xRu_xO$ Nanoparticles. A: x=0, B: x=0.005, C: x=0.01, D: x=0.04, E: x=0.08.

nanoparticles (x=0.005, 0.01, 0.04, 0.08) in this study[11]. The ability of the investigated samples $Ni_{1-2x}Mg_xRu_xO$ to store electrical energy is expressed by ε′, while the dielectric loss due to energy dissipation is indicated by ε′′. ε′ is calculated mathematically from the measured static capacitance C_p and the pellets' dimensions with an average area (A) of 127mm^2 and average thickness (t) of 2.74mm[12]. However, ε′′ is calculated from the tangent loss (tanδ) parameter[11].

For samples with x=0.04 and 0.08, a secondary phase appeared, which may cause an interaction at the interface (as grain boundary) between the main phase $Ni_{1-2x}Mg_xRu_xO$ and RuO_2. Figure 2 shows that higher ε′ and ε′′ values are observed at lower frequencies than at higher frequencies in some samples. $Ni_{1-2x}Mg_xRu_xO$ (x=0, 0.005, 0.01, 0.04, 0.08) nanoparticles notably record high real and imaginary dielectric values at high temperatures compared to lower temperatures. Grain boundaries are insulating, while in polycrystalline NiO-based materials, grains are typically semiconductors[13]. Therefore, at moderate temperatures, charges build up at grain boundaries and thus intensify polarization. Also, (Mg, Ru) dopants alter the grain boundary resistivity, influencing charge trapping and interfacial polarization.

3.2.1 Dopant Concentration Effects

XRD analysis shows that only samples with x=0.04 and 0.08 contain secondary RuO_2 phases, which create conductive interfaces within the NiO matrix that dominate the dielectric behavior. Furthermore, defects and dopant concentration effects play a significant role in the behavior of $Ni_{1-2x}Mg_xM_xO$. Mg^{2+} and Ru ions dopants form oxygen vacancies that act as charge compensation bases (charge trapping sites)[14]. Thus, more defects are introduced, boosting the dielectric permittivity at intermediate temperatures. For x<0.4, RuO_2 is fully dissolved as shown in the XRD results, Ru and Mg are likely still completely incorporated into the NiO lattice, which would maintain an optimized balance of defect-induced dipolar

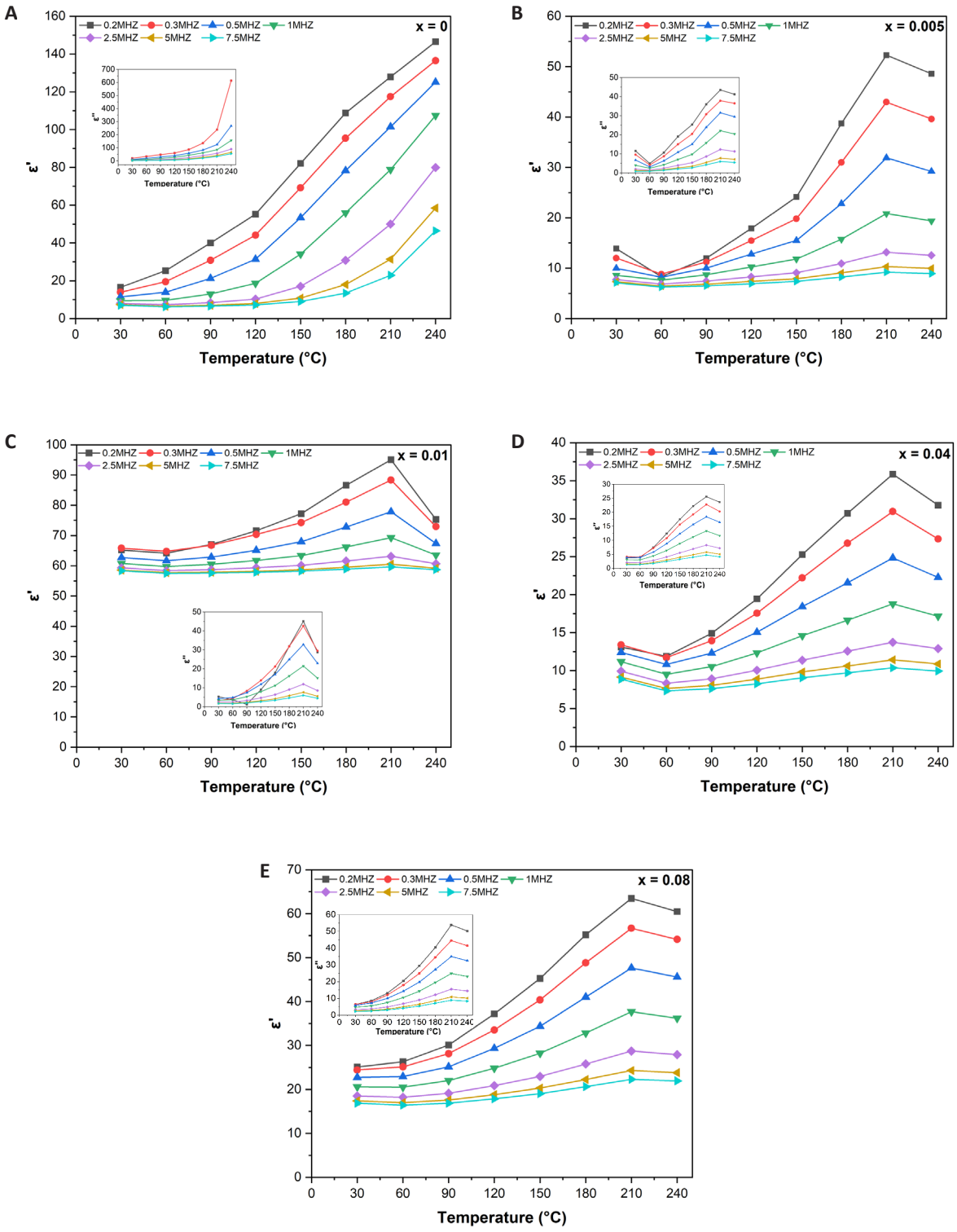


Figure 2. The Real and Imaginary Parts (Inset Figures) of the Dielectric Constant for $Ni_{1-2x}Mg_xRu_xO$ Nanoparticles as a Function of Temperature (30-240°C) at Selected Frequencies (0.2, 0.3, 0.5, 1, 2.5, 5, and 7.5MHz). A: x=0, B: x=0.005, C: x=0.01, D: x=0.04, E: x=0.08.

and space charge polarization, hence enhancing ε'. Dielectric constant values are highest at x=0.01 across all temperatures. At lower dopant concentrations, such as x=0.01, Ru probably creates uniformly distributed oxygen vacancies and mixed-valent states, both of which provide strong polarization mechanisms. Lower Ru quantity could alternatively improve the microstructure, intensify grain boundary density without phase blocking, and promote Maxwell–Wagner effective interfacial polarization when x=0.01. In contrast, for x =0.04 and x=0.08, the solubility limit of Ru and Mg was likely exceeded, and we likely see a degree of Ru segregation into the RuO_2 phase that limits the amount of active Ru ions within the lattice and reduces the direct contribution to polarization from substitutional doping[15]. The Maxwell-Wagner (MW) interfacial polarization explains the behavior of the dielectric constant in the context of space charge formation at low frequencies and as temperature

increases[10]. As temperature increases from 30-240°C, the samples containing RuO_2 exhibit a decrease in ε' and prominent ε'' peaks between 90-210°C, which correspond to thermally-activated interfacial charge accumulation and relaxation at NiO-RuO_2 boundaries. With the increase of the measured frequency, the ε'' peaks shift to higher temperatures due to Arrhenius-type dynamics[16]. For the x=0.08 sample, more intense polarization is shown due to greater interface density. In contrast, samples without RuO_2 display only broad, weak dielectric losses at temperatures higher than 180°C from intrinsic defects, which confirms that the RuO_2 secondary phase is essential for strong MW effects. Due to the temperature effect, a transition from interfacial polarization (90-180°C) to ohmic conduction (>180°C) shows how thermal energy changes charge transport mechanisms in these heterostructured materials[17].

Heavy doping at x=0.08 causes over-compensation, where excess defects act as recombination centers or traps, preventing dipoles from aligning and lowering ε′. With only 7.89% RuO_2, the x=0.08 sample may have more pronounced coarser secondary phase aggregates, leading to inactive electrical regions due to a lower surface-to-volume ratio. As a result of RuO_2 agglomeration, continuous highly conductive pathways begin to form through the sample x=0.08, which dampen the accumulation of charges at the interfaces, leading to a decrease in ε′ values compared to x=0.01. In addition, Figure 2D-E documents an increase in the dielectric values as the doping rises from 0.04 to 0.08, though both samples reported the existence of RuO_2 secondary phase. Although the amount of RuO_2 in the x=0.04 case was less (1.73%) than in x=0.08 (7.89%), the ε′ values in x=0.08 were greater, suggesting differences in microstructure and interfacial behavior. The x=0.08 sample had a higher volume percentage of RuO_2 and might have provided the NiO matrix with a semi-continuous or percolative network of RuO_2, which would have introduced a greater extent of conductive–insulating interfaces and more intense Maxwell–Wagner interfacial polarization. By contrast, the lower volume percentage of RuO_2 inclusions in the x=0.04 sample may not be enough to support significant interfacial charge accumulation via dense interfaces; the ensemble would then not enhance ε′. Also, once again, the grain boundary network in x=0.08 might have contained RuO_2 as a part of conductivity gradients; however, there may not have been enough Ru in x=0.04, which is insufficient to fully restructure that grain boundary effectively. The low amount of RuO_2 at x=0.04 might have even introduced charge trapping sites, increasing dielectric losses, without any concurrent interfacial gain. Ultimately, it seems reasonable that the x=0.08 sample is close to a percolation threshold, which facilitated long-range pathways for interfacial polarization, while x=0.04 remains behind this structural tipping point. Therefore, the sample with x=0.08 composition provides optimal adjustability for applications that need temperature-stable dielectric properties.

3.2.2 Temperature Dependence

Another point to consider is that charge carriers, such as electrons, holes, and ions, are thermally activated at low and moderate temperatures (30-210°C)[18]. Since NiO nanoparticles are p-type semiconductors, electrical conduction primarily occurs due to hole hopping between Ni^{2+} and Ni^{3+} sites[19]. The replacement of Ru^{4+} for Ni^{2+} ions creates a charge difference so that charge neutrality is maintained by oxidizing neighboring Ni^{2+} ions into Ni^{3+} ions, which in effect creates two Ni^{3+} sites for each Ru^{4+} dopant[20,21]. Similarly, substituting Mg^{2+} for Ni^{2+} creates cation vacancies, which supports further Ni^{3+} stabilization through insufficient Ni^{2+} ions that maintain charge neutrality[22,23]. Co-doping Ru^{4+} and Mg^{2+} enhances this effect, increases the hole concentration (Ni^{3+}), and suppresses Ni^{2+} recombination via strain relaxation due to Mg^{2+}'s slightly larger ionic radius (0.72Å). The concentration of Ni^{3+} increases the amount of polaron hopping between Ni^{2+} and Ni^{3+}, which is thermally activated and present as a dielectric relaxation process[24]. Additionally, the presence of the Mg^{2+} and Ru ions affects the charge carrier density, altering the charges' compensation mechanism[25,26]. As a result, as the temperature increases, more charge carriers gain thermal energy, leading to faster hole hopping and an increase in polarizability and ε′.

The relaxation behavior can be observed in the dielectric data collected as a function of temperature at certain frequencies. However, at 210°C, both dielectric constants reach a peak, designating a resonance or what is known as a relaxation phenomenon. Additionally, the 4.3% ionic radius mismatch between Mg^{2+} (0.72Å) and Ni^{2+} (0.69Å) introduces local lattice strain that modifies the potential landscape around Ni^{2+}/Ni^{3+} hopping sites, likely contributing to the defect trapping environment that governs the onset of this relaxation peak in doped samples. As shown in Figure 2B-E, a strong peak or anomaly in ε′ with temperature often reveals the relaxation process or transition in the mechanism of polarization at intermediate temperatures, first indicated by the upward trend. In ε″ (imaginary part) vs temperature plots, the peaks were also evident at specific temperatures due to maximum energy dissipation as a function of hopping between Ni^{2+} and Ni^{3+}. This behavior may be attributed to one of two possibilities. First, a structural transition may have occurred due to the nature of some NiO-based nanomaterials, which shift from a polarized (ferroelectric state) to a non-polar (paraelectric state) at around 200-250°C[25,27]. Local structural distortions, formed by Mg and Ru dual doping, create local polar regions. However, as the temperature increases, this pseudo-ferroelectric regime breaks down and becomes a paraelectric-like system where thermal

perturbations suppress continuous dipole alignment. Second, the $Ni_{1-2x}Mg_xRu_xO$ (x=0.005, 0.01, 0.04, 0.08) system hits an optimal state where the charge carriers orient effectively with the alternating electric field and hit the maximum response, which is identified as the relaxation of space charge polarization[28].

3.2.3 Frequency Dependence

According to Figure 2B-E, it is noticed that the increase and decrease in both dielectric constants are sharper and have larger values at lower frequencies (0.2-1MHz) than at high frequencies (1-7.5MHz). The average rate of increase in the real part of the dielectric constant values at x=0.005 between 0.2 and 1MHz is 9.56%, while 2.98% in the range (1-7.5MHz). Similarly, as ε′ decreases from 210 to 240°C, the average rate of decrease at lower frequencies (0.2-1MHz) is 9.32% and 2.25% at higher frequencies (1-7.5MHz). This trend is also notable for ε′′, where the percentage of increase is 14.25 in the range (0.2-1MHz), whereas it is 2.01% at higher frequencies from 1 to 7.5MHz. Also, as ε′′ drops, the rate is 6.19% between 0.2 and 1MHz, while 3.19% is in the range (1-7.5MHz). This behaviour is also significant in all other dopant concentrations. All polarization mechanisms (space charge, dipolar, ionic, and electronic) occur at low frequencies (0.2-1MHz), where space charge and interfacial polarization dominate[4]. Localized or defect polarizations result from the accumulation of charge carriers (electrons, holes, or ions) at interfaces, grain boundaries, or defects. Additionally, because of their smaller grain size than in their bulk condition, NiO nanoparticles typically have a high density of grain boundaries[30]. Thus, in conjunction with Koop's phenomenological theory, it increases charge accumulation and contributes to interfacial polarization (Maxwell-Wagner Effect)[4]. Pure NiO may naturally exhibit all these structural deformations, or dual doping of (Mg, Ru) nanoparticles may intensify them. Therefore, the polarization effect is larger at higher doping doses. The charges will readily react and align with the field, creating dipolar polarization because of the slow oscillations of the electric field. Moreover, ion displacements inside the lattice of pure and dual-doped NiO nanoparticles and the distortion of electron clouds, respectively, cause ionic and electronic polarizations[4]. High ε′′ values are thus described by energy lost from charge carrier motions and relaxation processes. However, at high frequencies (1-7.5MHz), since electric field oscillations are rapid that charge carriers can no longer align and follow them, electronic and ionic polarizations are the only dominating polarizations with comparatively small or constant effects at this level[4]. Since the charge carriers won't have enough time to migrate, aggregate, and align with the external alternating electric field, even defects stop substantially contributing to polarization at high frequencies. As a result of reduced polarization mechanisms, the decrease in ε′′ indicates a depletion in energy loss.

By referring to Figure 2A, it is well-documented that the pure NiO nanoparticles undergo a considerable increase in both dielectric constants as the temperature increases from room temperature to 240°C without showing any peak or drop at certain points. A similar study conducted in 2017 also revealed the same behavior of ε′ and ε′′ in response to frequency variations, stressing the effect of temperature on increased dielectric constants[31]. This rise in the real part of the dielectric constant is attributed to the frequency and temperature dependence of the sample. At lower frequencies (0.2-1MHz), space charge polarization is enhanced, and as temperature increases from 30 to 240°C, dipolar polarization becomes thermally activated, resulting in a rise in ε′ values. However, at higher frequencies (1-7.5MHz), charge carriers fail to align with the alternating electric field, which is shown in lower ε′ values than those at lower frequencies. This monotonic rise in the ability of NiO nanoparticles to store electric energy without showing any peak is due to the absence of defect states caused by adding dopants. Accordingly, the charge carriers won't be trapped and will continue their contribution to polarization at all temperatures. As a result, ε′′ values will also continue to increase since the resistance of grain boundaries in this case reduces, and conductivity losses dominate.

Overall, all the samples being studied are temperature and frequency-dependent. However, compared to pure NiO nanoparticles, $Ni_{1-2x}Mg_xRu_xO$, where x=0.005, 0.01, 0.04, and 0.08, showed a different response to the change in frequency and temperature. ε′ in pure NiO nanoparticles records a minimum of 7.050 at 30°C and 7.5MHz and a maximum of 146.489 at 240°C and 0.2MHz. However, among the (Mg, Ru) dual-doped NiO nanoparticles, ε′ exhibits the least value of 7.095 at 30°C and 7.5MHz for x=0.005 and a highest value of 75.286 at 210°C and 0.2MHz for x=0.01. The minimum value of ε′′ occurs at 30°C and 7.5MHz with a value of 1.699 for x=0 and 0.816 for x=0.005. On the other hand, pure NiO nanoparticles achieve a maximum of 614.076 at 240°C and 0.2MHz, while for $Ni_{1-x}MgRu_xO$, at 210°C and 0.2MHz, a maximum of 53.885 occurs for x=0.08. Note that for x=0.04 and x=0.08, the ε′ and ε′′ values documented in this section show composite measurements of the NiO–RuO_2 heterostructure, as no effective medium correction was applied to isolate the NiO matrix contribution. A quantitative EIS-based decomposition isolating the grain-interior and interfacial permittivity components for these samples is provided in Section 4.5.

3.3 AC Conductivity vs. Temperature and Frequency

Figure 3B-E illustrates a significant increase in AC conductivity as the temperature increases from 30°C and peaks at around 210°C, followed by a drop for all

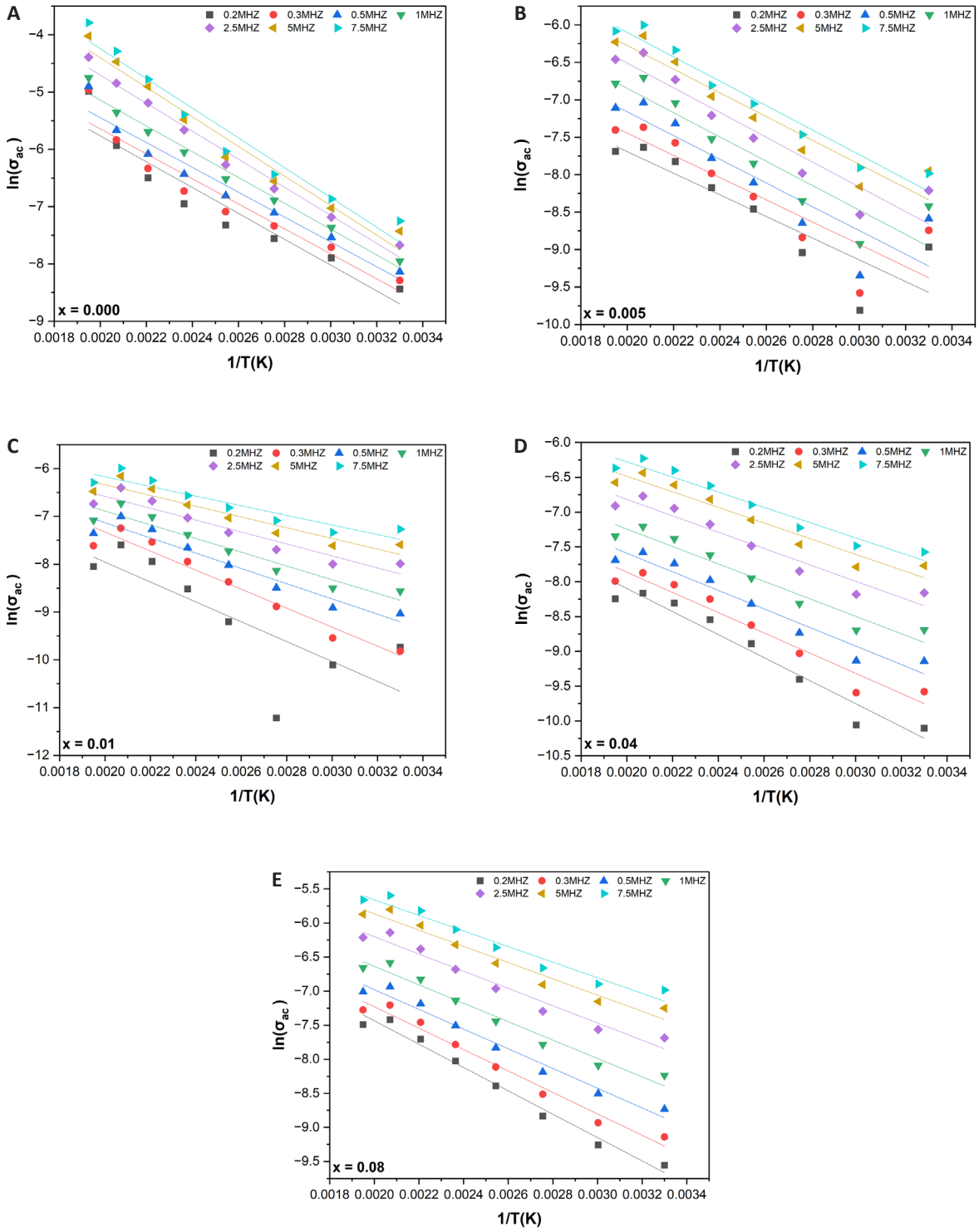


Figure 3. Fitting Plots of the Activation Energy (E_a) for $Ni_{1-2x}Mg_xRu_xO$ Nanoparticles as a Function of Temperature (30-240°C) at Selected Frequencies (0.2, 0.3, 0.5, 1, 2.5, 5, 7.5MHz). A: x=0, B: x=0.005, C: x=0.01, D: x=0.04, E: x=0.08.

dopant concentrations at selected frequencies (0.2, 0.3, 0.5, 1, 2.5, 5, 7.5 MHz). The opposite of resistivity is AC conductivity, which measures a material's electrical conduction capacity or its ability to permit current flow. The concentration of the charge carriers ($N=N_e + N_h$), which are electrons or holes, and their mobility are directly correlated with AC conductivity denoted by σ_{ac}[32]. AC conductivity is calculated using the following equation[33]:

$$\sigma_{ac} = \omega\varepsilon'\varepsilon'' \quad (1)$$

For whichΩ is the angular frequency.

The conductivity variations with frequency are expressed as:

$$\sigma = \sigma_{dc} + \sigma_{ac} \quad (2)$$

For which σ_{dc} designates the DC conductivity and σ_{ac} shows the AC conductivity.

Since $Ni_{1-2x}Mg_xRu_xO$ are considered to be semiconducting

Table 1. Values of the E_a for $Ni_{1-2x}Mg_xRu_xO$ (x=0, 0.005, 0.01, 0.04, 0.08) Nanoparticles at Selected Frequencies (0.2, 0.3, 0.5, 1, 2.5, 5, 7.5MHz) Within the Temperature Range (30-240°C)

	E_a (eV)				
	x=0	**x=0.005**	**x=0.01**	**x=0.04**	**x=0.08**
0.2MHz	0.1943	0.15094	0.17374	0.14249	0.14771
0.3MHz	0.18801	0.16213	0.17148	0.12518	0.13554
0.5MHz	0.18688	0.17728	0.13722	0.11478	0.12473
1MHz	0.19415	0.183	0.12357	0.10788	0.11644
2.5MHz	0.21099	0.17827	0.09054	0.10121	0.10916
5MHz	0.22227	0.13662	0.11523	0.0967	0.10272
7.5MHz	0.22384	0.14075	0.11617	0.09411	0.0986

materials, then σ_{ac} follows the Arrhenius-type temperature dependence at a constant frequency, which is expressed by the following equation[34]:

$$\sigma_{ac}(T)=\sigma_o\exp(^{-E_a}/_{k_bT}) \quad (3)$$

For which σ_o is the pre-exponential factor, E_a is the activation energy needed for the charge carriers to contribute to conduction, E_b is Boltzmann's constant, and T is the temperature.

The data of the activation energy (E_a), shown in Table 1, reflect the thermal energy barrier that charge carriers must overcome to be involved in conduction in pure and (Mg, Ru) co-doped NiO samples over the frequency range of 0.2-7.5 MHz. In pure NiO (x=0), Ea increases with frequency, ranging from 0.194eV at 0.2MHz to 0.223eV at 7.5MHz. The increase in E_a as a function of frequency reveals that conduction at higher frequencies involves longer-range hopping between deeper localized states, which requires a higher E_a without the interference of dopant-induced defect levels[35]. In doped samples (x=0.005–0.08), however, there is an opposite trend, where E_a decreases systematically with increasing frequency. For example, E_a drops from 0.147eV at 0.2MHz to 0.098eV at 7.5MHz in the x=0.08 sample. This indicates that co-doping with Mg^{2+} and Ru^{4+} generates shallow defect states in the NiO bandgap, creating lower energy thresholds that allow thermally activated short-range hopping. These states originate from charge imbalance and lattice distortion, enabling phonon-assisted polaron hopping to occur between Ni^{2+} and Ni^{3+} sites[36]. Additionally, increasing dopant concentration decreases E_a over all frequencies, indicating that pathways for localized hopping conduction continue to develop as the sample is doped[4]. One significant aspect about the x=0.04 and x=0.08 samples is the detection of RuO_2 as a secondary phase, accounting for 1.73% and 7.89% of the overall sample weight, respectively, determined via X-ray diffraction. RuO_2, as a highly conductive oxide, has a more specific role in the conduction process. At medium levels of Mg and Ru dopant concentration (x=0.04), RuO_2 acts as an extrinsic conductive pathway, thus promoting higher overall conductivity through connecting poorly conducting grain boundaries or aiding the interfacial transport process. This aligns with the defect-assisted hopping mechanism in the host NiO lattice and results in the lowest E_a (0.094eV at 7.5MHz) and highest AC conductivity amid the doped samples. However, in the case of the x=0.08 sample, in which the RuO_2 phase fraction is 7.89%, there is a partial counterbalance taking place. The excess of Ru is segregating into the secondary phase to a degree that is limiting the Ru^{4+} substitution into the NiO lattice and thus limiting the formation of Ni^{3+} and availability of internal hopping centres[37]. Therefore, the x=0.08 sample has the highest absolute AC conductivity value (0.003 S/m at 210°C and frequency of 7.5MHz) but at a slightly higher E_a than the x=0.04 sample. This suggests that after a certain amount of phase separation, the RuO_2 acts more as an inert phase, detracting from the added benefits of co-doping, hence causing the contribution to be negligible to defect-mediated conduction within the NiO matrix.

Figure 4 shows the temperature-dependent AC conductivity behavior of pure and co-doped NiO nanoparticles at selected frequencies from 0.2 to 7.5MHz. The AC conductivity for all the samples increased with temperature, reaching a maximum at approximately 210°C, then experiencing a clear decline beyond that point. This non-monotonic behavior was particularly evident for the doped samples as seen in Figure 4B-E, whereas the pure NiO, as shown in Figure 4A, only showed a continuous rise without declining, which implied a different conduction process in the presence of Mg and Ru dopants. The increase in σ_{ac} with temperature is due to the thermally activated hopping of charge carriers, predominantly small polarons, between localized defect states induced by the Mg^{2+} and Ru^{4+} dopants[38]. The defects introduce mid-gap states in the NiO lattice that can assist in phonon-activated hopping, therefore enhancing conductivity with increasing temperatures[39]. Additionally, this increase is frequency-dependent; at higher frequencies, such as 7.5MHz, the energy is adequate to couple the carrier dynamics with oscillating electric fields, resulting in higher σ_{ac} than at lower frequencies (0.2MHz). The peak observed at 210°C across all doped samples indicates a temperature limit where thermal enhancement of carrier mobility begins to break down due to competing mechanisms[40]. Beyond

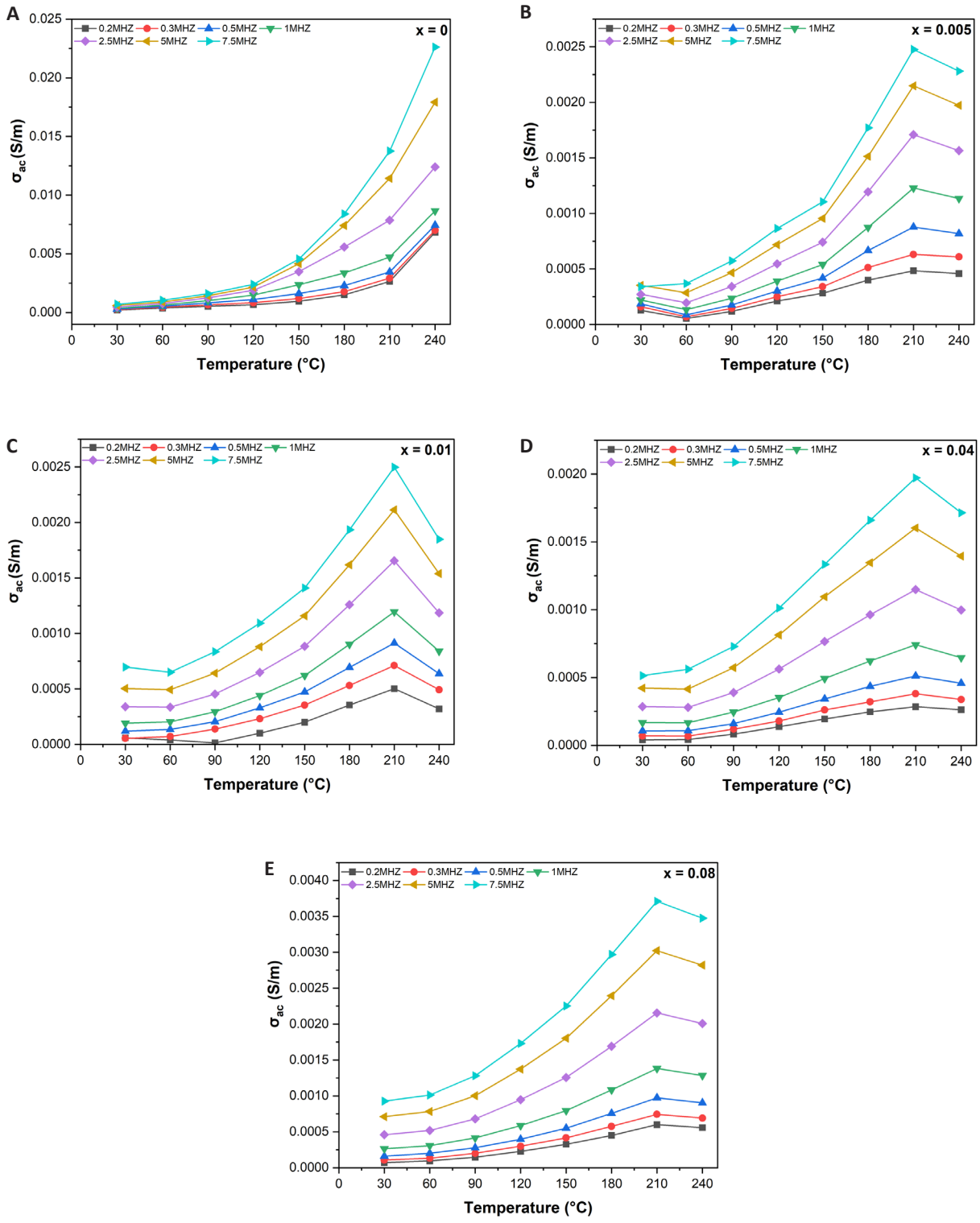


Figure 4. AC Conductivity for $Ni_{1-2x}Mg_xRu_xO$ Nanoparticles as a Function of Temperature (30-240°C) at Selected Frequencies (0.2, 0.3, 0.5, 1, 2.5, 5, 7.5MHz). A: x=0, B: x=0.005, C: x=0.01, D: x=0.04, E: x=0.08.

this limit, σ_{ac} decreases, indicating scattering of carriers and decreased mobility overall. There are several considerations for this observed behaviour[41,42]. One, excessive phonon scattering at structurally elevated temperatures, which conflicts with polaron hopping by inducing carrier-lattice coupling. Two, the formation of ionic secondary phases (RuO_2), which decreases conduction as a result of phase segregation. The x=0.08 sample shows the highest σ_{ac} value (0.003S/m at 210°C, 7.5MHz), suggesting a synergistic contribution of Mg and Ru doping at moderate temperatures. While the highest σ_{ac}values were found for this sample, it also showed the steepest decline in conductivity after 210°C, likely due to phase instability or heterogeneous segregation of RuO_2, thus limiting higher improvement of charge carrier transport. According to Figure 4A, AC conductivity in pure NiO nanoparticles undergoes a monotonic increase as the temperature rises from 30 to 210°C without showing any peak. This behavior can be attributed to thermally activated charge carriers that hop between localized

Table 2. Values of the Exponent s(T) and R^2 for $Ni_{1-2x}Mg_xRu_xO$ (x=0, 0.005, 0.01, 0.04, and 0.08) Nanoparticles at Selected Temperatures within a Frequency Range (0.1-8MHz)

	T (°C)	30	60	90	120	150	180	210	240
x=0	s(T)	0.32071	0.25715	0.26852	0.30559	0.39196	0.47055	0.48419	0.37925
	R^2	0.99182	0.97790	0.95454	0.94031	0.96026	0.99013	0.98489	0.92568
x=0.005	s(T)	0.25881	0.45994	0.40348	0.37239	0.36392	0.37812	0.40515	0.39963
	R^2	0.95696	0.95041	0.97810	0.99297	0.99879	0.99221	0.97910	0.98077
x=0.01	s(T)	0.67671	0.67280	0.51274	0.50363	0.44118	0.40453	0.39187	0.42089
	R^2	0.98890	0.96031	0.99549	0.96504	0.98079	0.98824	0.99048	0.98738
x=0.04	s(T)	0.55064	0.56454	0.52482	0.50506	0.48945	0.48724	0.49230	0.48833
	R^2	0.93693	0.94038	0.96719	0.98299	0.99110	0.99641	0.99728	0.99742
x=0.08	s(T)	0.59496	0.56458	0.53660	0.51902	0.50431	0.49412	0.48433	0.48663
	R^2	0.95996	0.97376	0.98324	0.99134	0.99485	0.99723	0.99781	0.99776

states, resulting in a continuous increase in $\sigma_{ac.}$ The absence of a peak in pure NiO nanoparticles indicates no phase transition or scattering effects by induced dopants and minimal interference of state defects[43]. σ_{ac} hits a maximum of 0.022S/m at 240°C and 7.5MHz and a minimum of 2.162E-4 S/m at 30°C and 0.2MHz.

Another point to consider is the significant growth of σ_{ac} as the frequency increases, where AC conductivity exhibits high values at 7.5MHz compared to those at 0.2 MHz across all dopant concentrations. This enhancement in AC conductivity with frequency is consistent with Jonscher's Universal Power Law expressed by the following equation[33]:

$$\sigma_{ac}(\omega)=A(T)\omega^{s(T)} \quad (4)$$

The exponent s(T) (0<s<1) is a temperature and material-dependent parameter associated with the degree of interaction between mobile ions and the lattice. A(T) is a temperature-dependent parameter indicating the strength of polarizability.

Table 2 shows the values of s(T) for all dopant concentrations. This exponent indicates the dominating conduction mechanism and the interaction strength between the mobile carriers and the lattice. In pure NiO (x=0), s(T) increased in value from 0.32 at 30°C to a maximum value of 0.48 at 210°C. This is a typical behavior of Correlated Barrier Hopping (CBH) in which conduction involves carriers hopping over potential barriers that become increasingly significant with increased temperature[44]. All dual-doped samples (x =0.005-0.08) showed a decreasing or nearly constant s(T) with increasing temperature. In the case of the x=0.01 sample example, s(T) dropped from 0.67 at 30°C to 0.39 at 210°C. In the x=0.08, the decrease in s(T) was from 0.59 and 0.48 over the same temperature range. The monotonic decrease (or stabilizing) of s(T) with temperature suggests a Small Polaron Hopping (SPH) mechanism, since increased thermal energy likely lowers the activation barrier for hopping and increases the frequency of hopping transitions between localized states[45]. This behavior confirms the contribution of the Mg and Ru dopant-created shallow energy levels to enhancing short-range carrier mobility. Furthermore, the nearly constant s(T) values in x=0.04 and x=0.08 at higher temperatures (0.48-0.49) hint at a partial contribution from Quantum Mechanical Tunneling (QMT) at high frequencies and disordered levels. QMT is an important consideration when hopping transitions can occur in combination with tunneling through thin energy barriers, particularly for disordered lattices at high frequencies[46] (Figure 5).

Based on AC conductivity, frequency exponent s(T) and E_a behavior, as discussed, the conduction mechanism for (Mg, Ru) co-doped NiO nanoparticles can be identified as Small Polaron Hopping (SPH). The data support the SPH mechanism through the systematic decrease of s(T) with temperature due to the peak in conductivity around 210°C and the drop in Ea with increasing frequency and Mg and Ru dopants, respectively. The observations made in the cases of pure NiO nanoparticles do not support the SPH mechanism, since the behavior of pure NiO suggests a fast increase in E_a with frequency and an increase of s(T) with temperature. The highly disordered, or heavily doped samples, may have a small contribution from Quantum Mechanical Tunneling (QMT) effects, observed at high frequencies; however, it is secondary to the SPH contribution for temperatures below 210°C.

3.4 Loss Tangent vs. Temperature and Frequency

The dielectric loss tangent (tan δ) describes the energy dissipation in a dielectric and is dependent on two main contributors: polarization mechanisms and electrical conductivity. The presence of temperature-dependent peaks, shown in Figure 6, in the tanδ at higher temperatures, alongside varying trends at lower temperatures, characterized the dielectric loss behavior of pure NiO and (Mg, Ru) co-doped NiO across a temperature range of 30°C to 240°C and frequencies from 0.2MHz to 7.5MHz.

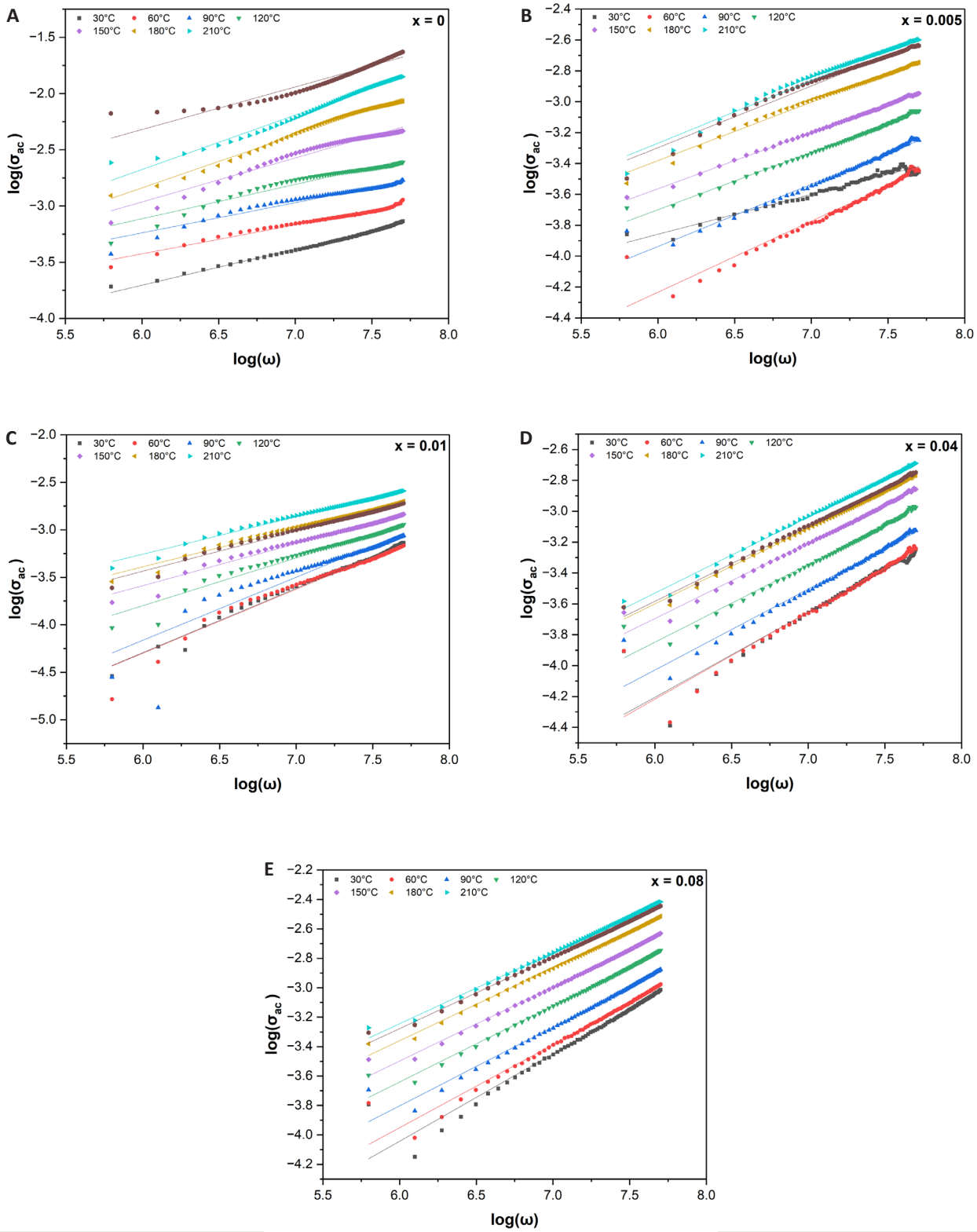


Figure 5. Fitting Plots of the Temperature-dependent Exponent s(T) for $Ni_{1-2x}Mg_xRu_xO$ Nanoparticles as a Function of Temperature (30-240°C) at Selected Frequencies (0.2, 0.3, 0.5, 1, 2.5, 5, 7.5MHz). A: x=0, B: x=0.005, C: x=0.01, D: x=0.04, E: x=0.08.

tan δ of pure NiO (x=0), shown in Figure 6A, demonstrates a continuous gradual rise with temperature up to about 180°C, followed by a sharp increase at higher temperatures, particularly at lower frequencies, which can be attributed to activation of significant loss mechanisms such as shifted conduction and space charge polarization[47]. At lower temperatures, tan δ tends to remain more stable as there are fewer thermally activated charge carriers available to move around. At 30°C and 7.5MHz, the minimum tan δ value of 0.241 indicates that dielectric losses (dissipation factor) are limited due to low thermal agitation. At 240°C and 0.2MHz, there is a peak tan δ value of 4.191, indicating that conduction-related losses dominate due to thermally activated hopping of charge carriers and increased interfacial polarization. In contrast, in Figure 6B-6E, the co-doped samples displayed more complicated temperature

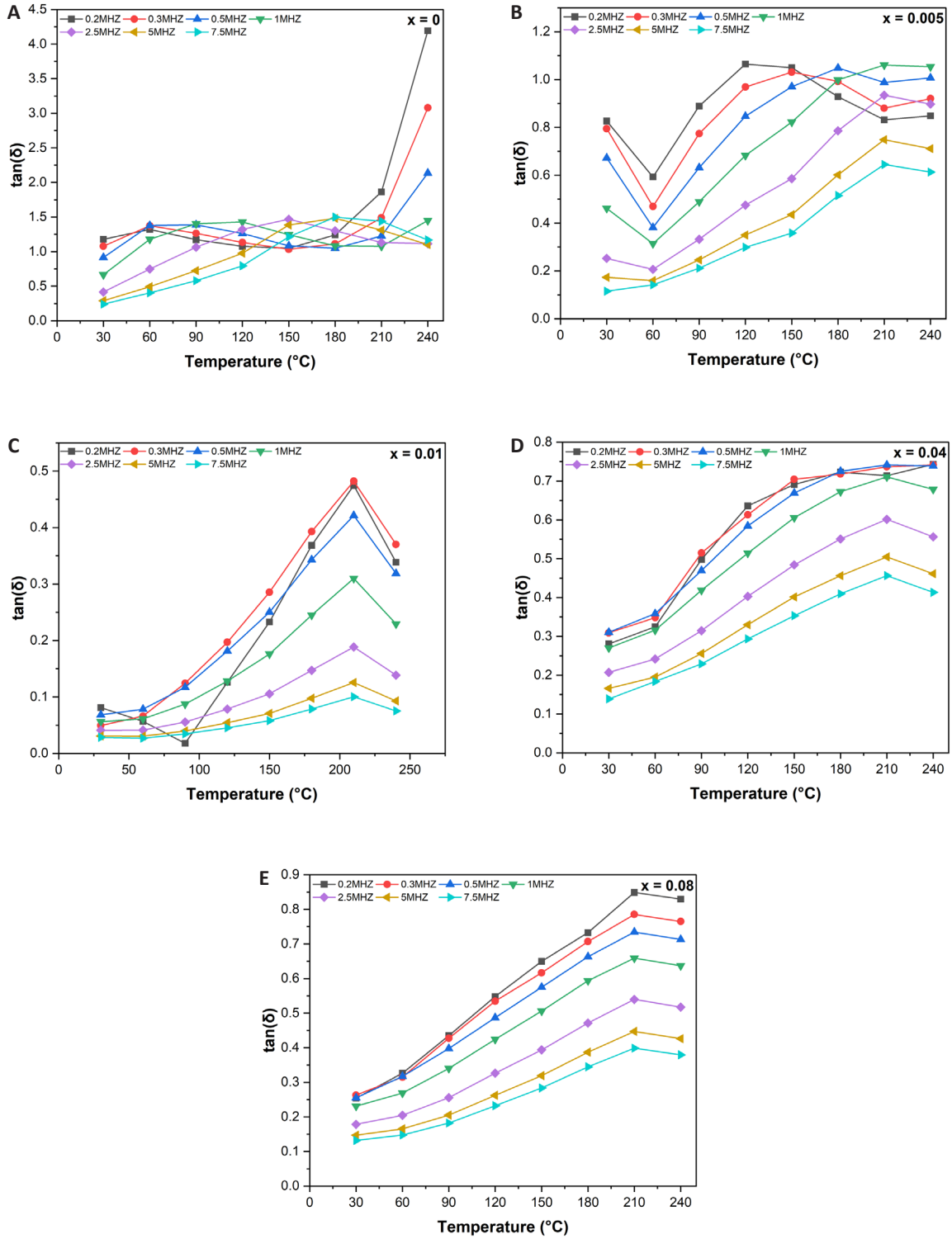


Figure 6. Tan δ for $Ni_{1-2x}Mg_xRu_xO$ Nanoparticles as a Function of Temperature (30-240°C) at Selected Frequencies (0.2, 0.3, 0.5, 1, 2.5, 5, 7.5MHz). A: x=0, B: x=0.005, C: x=0.01, D: x=0.04, E: x=0.08.

and frequency dependencies due to the addition of Mg^{2+} and Ru^{4+} to the NiO lattice. The sample with a dopant concentration of x=0.005 exhibits a distinctive minimum in tan δ near 60°C across different frequencies, indicating a possible transition in the process dominating the relaxation, changing from dipolar or interfacial processes to hopping-related processes. However, as the temperature increases further, tan δ increases gradually, indicating that thermally assisted relaxation mechanisms are in progressively increasing degrees of activation. The x=0.01 sample displayed the sharpest minimum of tan δ of 0.018 at 90°C and 0.2MHz, which is much lower compared to the other samples. The minimum tan δ likely indicates increased dielectric stability with temperature, possibly because too many charge carriers are localized or there is negligible conduction due to defects. The dip in tan δ suggests an increased dielectric stability before 150°C due to maximal charge carrier's localization or weak defect conduction. For temperatures above 150°C, there is a relatively broad peak centered approximately on 200°C that appears at lower frequencies and indicates the presence of strongly thermally activated relaxation processes that may involve

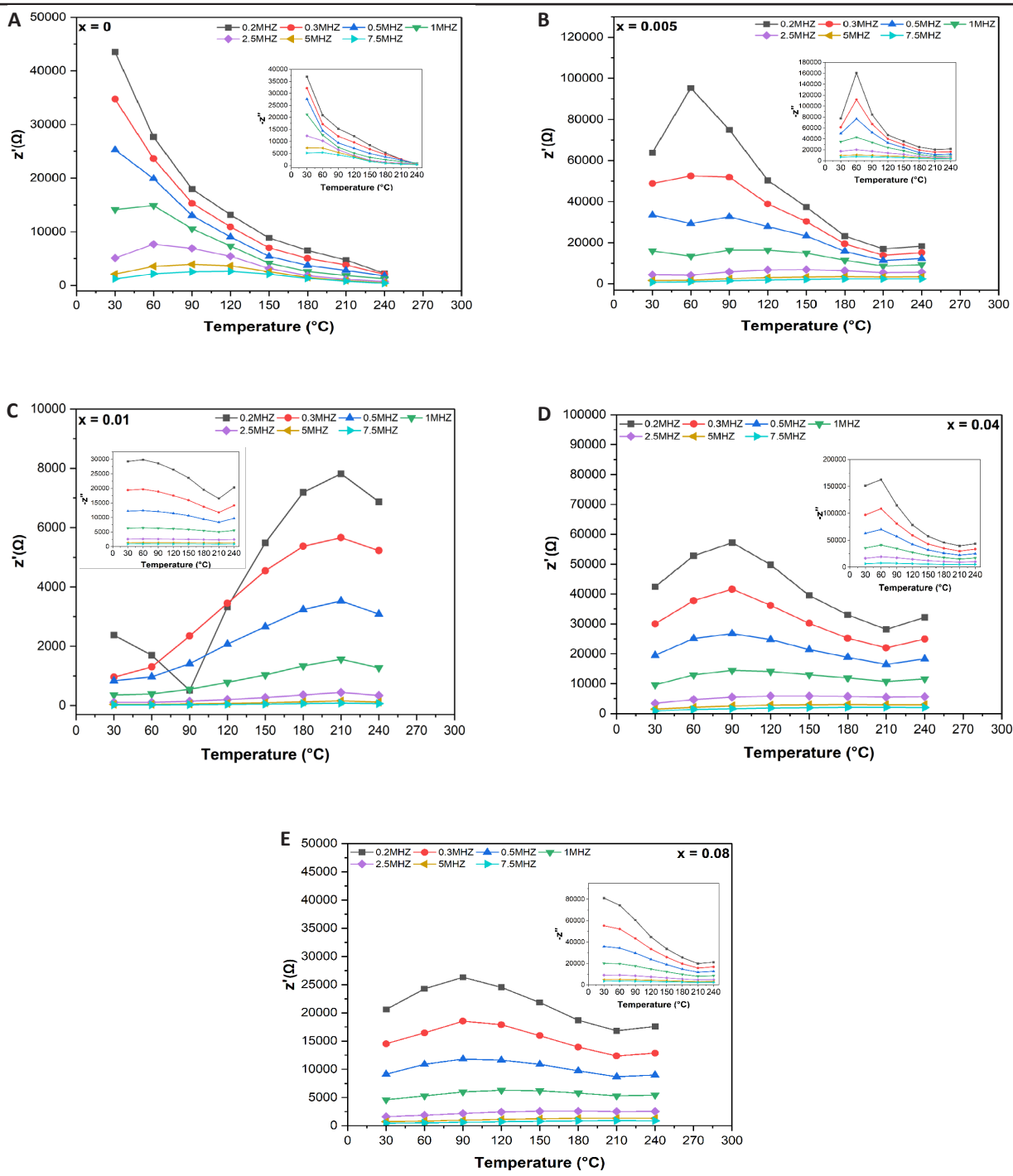


Figure 7. The Real and Imaginary Parts (Inset Figures) of the Impedance for $Ni_{1-2x}Mg_xRu_xO$ Nanoparticles as a Function of Temperature (30-240°C) at Selected Frequencies (0.2, 0.3, 0.5, 1, 2.5, 5, 7.5MHz). A: x=0, B: x=0.005, C: x=0.01, D: x=0.04, E: x=0.08.

space charge accumulation at grain boundaries or polaron hopping. Both x=0.04 and x=0.08 samples containing an elevated level of doping exhibit a gradual increase in tan δ with temperature, yet do not indicate a minimum. However, a noticeable broad peak was found around 210°C at lower frequencies, suggesting a thermally activated relaxation process related to the increase in defect concentration due to high dopant levels. Sample x=0.08 exhibits the maximum value of tan δ among the rest of the samples with a value of 0.848 at 240°C and 0.2MHz, notably lower than pure NiO nanoparticles. This illustrates that co-doping provided changes to charge carrier dynamics, either limiting mobility or restricting conduction at grain boundaries. The tan δ decreased with increasing frequency in all studied samples, revealing the frequency dependence of polarization mechanisms. At high frequencies, dipolar or interfacial dipoles are unable to reorient rapidly enough to keep up with the alternating electric field, and therefore their energy loss is diminished. At lower frequencies, these contributions become more relevant, as the polarizations are more active, and especially conduction contributions, which have the most significance at elevated temperatures. The changes in tanδ observed as a function of temperature and for different doping concentrations reveal the role played by the co-doping of Mg and Ru on dielectric losses in NiO nanoparticles, which possibly can be attributed to

changes in defect chemistry, conductivity, and space charge polarization. Peaks observed at particular temperatures suggest the activation of thermally activated relaxation processes, which appear strongly dependent on the dopant concentration and frequency[4,8,48].

3.5 Impedance vs. Temperature and Frequency

Figure 7 shows that while pure NiO nanoparticles have a simple form of semiconducting behavior, with both real and imaginary parts of impedance decreasing with increasing temperature due to increased charge carrier activation, the (Mg, Ru) co-doped NiO samples exhibit non-linear behaviors that have more complicated inter-relation between dopant-induced defect states, modified grain boundary barriers, and dielectric relaxation processes. Leveraging their application, the impedance of the samples under investigation reveals complexity, denoted by Z*, when subjected to an AC electric field, where the reactive and resistive components were calculated mathematically[49].

In pure NiO, the rising temperature boosts carrier mobility, thus reducing resistive losses and capacitive polarization[50]. However, there would be higher barrier potentials at the grain boundaries in the doped samples due to the creation of additional defect states and a change in microstructure as a result of the introduction of Mg and Ru ions; this is evidenced in the case of the x=0.005 sample where initially at 90°C, the real part of impedance rises, suggesting that these barriers are temporarily hindering charge transport before dropping off as thermal energy surpasses the barriers up to about 210°C[6]. From there on, the impedance rises again, most probably because of other thermal phenomena; this could also be due to microstructural changes or additional scattering phenomena. The imaginary portion in this sample showed analogous trends but peaks somewhat earlier (approximately at 60°C), implying that the dielectric relaxations, which are invoked via the polarization mechanisms at the interfaces, possess relatively lower activation energies for the contributive processes toward the resistive component[51]. The real part, Z′, of the x=0.01 sample increases with increasing temperature up to 210°C, possibly due to continuous dopant-induced scattering or the presence of dopant-induced trap states, which enhance resistance and then decrease upon further thermal activation. However, the imaginary part behaves quite differently by decreasing until 210°C and then rising in the activated frequency range, attributed to the changes in interfacial polarization. The same trends are also observed in the x=0.04 and 0.08 samples; initially, both the real and imaginary parts show an increase until about 90°C, followed by a decrease toward 210°C, and then rise again. This indicates that concentrations of higher dopants promote defect and boundary effects at lower temperatures; however, as the temperature rises, these effects lessen due to increased carrier mobility until impeding influences exert further structural changes induced by thermal fluctuations, ultimately resulting in impedance changes again[6]. Such behaviour demonstrates how (Mg, Ru)- co-doped NiO nanoparticles, thermally activated processes, dopant-induced modifications to the crystal structure, and dielectric relaxation mechanisms due to frequency dependence unite and interact to govern the impedance behaviour, making it extraordinarily more complex than in pure NiO.

Another point to consider is that the impedance Z′ and |Z′′| of pure NiO and $Ni_{1-2x}Mg_xM_xO$ nanoparticles are greater at low frequencies (0.2-1MHz) compared to high frequencies (1-7.5MHz), as reported in Figure 7. The real part of the impedance Z′, the resistive component, is higher at lower frequencies because the charge carriers contributed by Mg and Ru dopants, i.e., holes, cannot easily overcome the grain-boundary resistance and defects[52]. However, at high frequencies, charge carrier hopping becomes significant and has sufficient energy from the AC field to overcome the resistivity of the grain boundaries and move more freely[46]. In addition, the imaginary part of the impedance |Z′′|, the reactive component, tends to be higher at low frequencies due to the accumulation of charge carriers at the interfaces (space charge effects), contributing to effective polarization[53]. However, at higher frequencies, polarization decreases as the charge carriers cannot follow the rapid oscillations of the electric field, and the capacitive reactance decreases; thus, the reactive component decreases[53]. Moreover, charge carrier dynamics change with the increase of frequency. At low frequencies, charge carriers become trapped in localized defect states, thereby raising impedance, while at high frequencies, charge carriers have no time to become trapped, thus decreasing impedance[54].

At 30°C and 0.2MHz, Z′ and |Z′′| for pure NiO nanoparticles hit a maximum of 413.426 and 36961.744Ω, respectively. While at 210°C and 7.5MHz, Z′ and |Z′′| report a minimum of 413.426 and 353.86Ω, respectively. However, among (Mg, Ru) dual-doped NiO nanoparticles, a maximum of Z′ of 95314.631Ω occurs at x=0.005, 60°C, and 0.2MHz, while at x=0.01, 30°C, and 7.5MHz, a minimum of 25.061 appears. |Z′′| hits a maximum of 162695.587Ω for x=0.04, at 60°C and 0.2MHz, and a minimum value of 864.621Ω at x=0.01, 240°C, and 7.5MHz.

The dielectric properties of NiO nanoparticles and co-doped NiO nanoparticles in (Mg, Ru) were studied by impedance spectroscopy, where x=0, 0.005, 0.01, 0.04, and 0.08. The Nyquist plots (|Z′′| vs. Z') were plotted over the wide temperature range of 30-240°C to understand the impedance behavior and to clarify the role of temperature on the dielectric characteristics of the reported samples. The Nyquist plots obtained were fitted using Electrochemical Impedance Spectroscopy (EIS) Spectrum Analyzer software, as shown in Figures 8-12

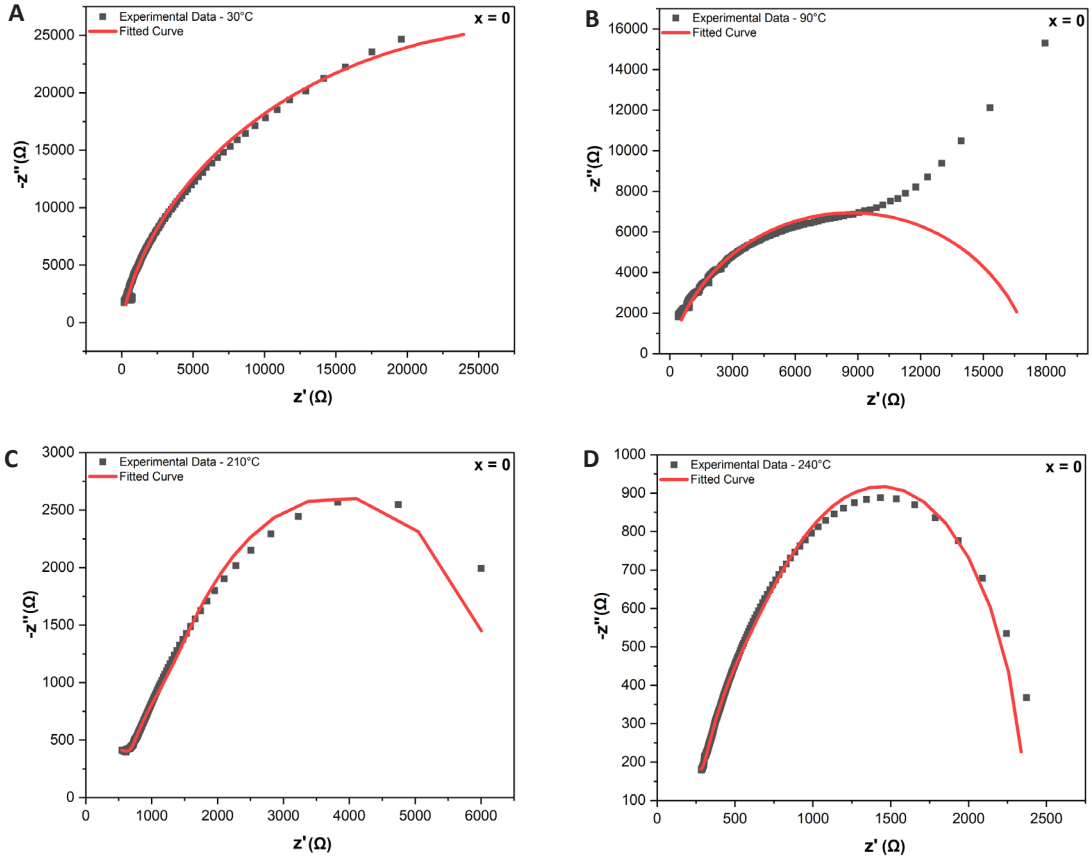


Figure 8. Nyquist Plots for Pure NiO Nanoparticles as a Function of Frequency (0.1-8MHz) at Selected Temperatures. A: 30°C, B: 90°C, C: 210°C, D: 240°C.

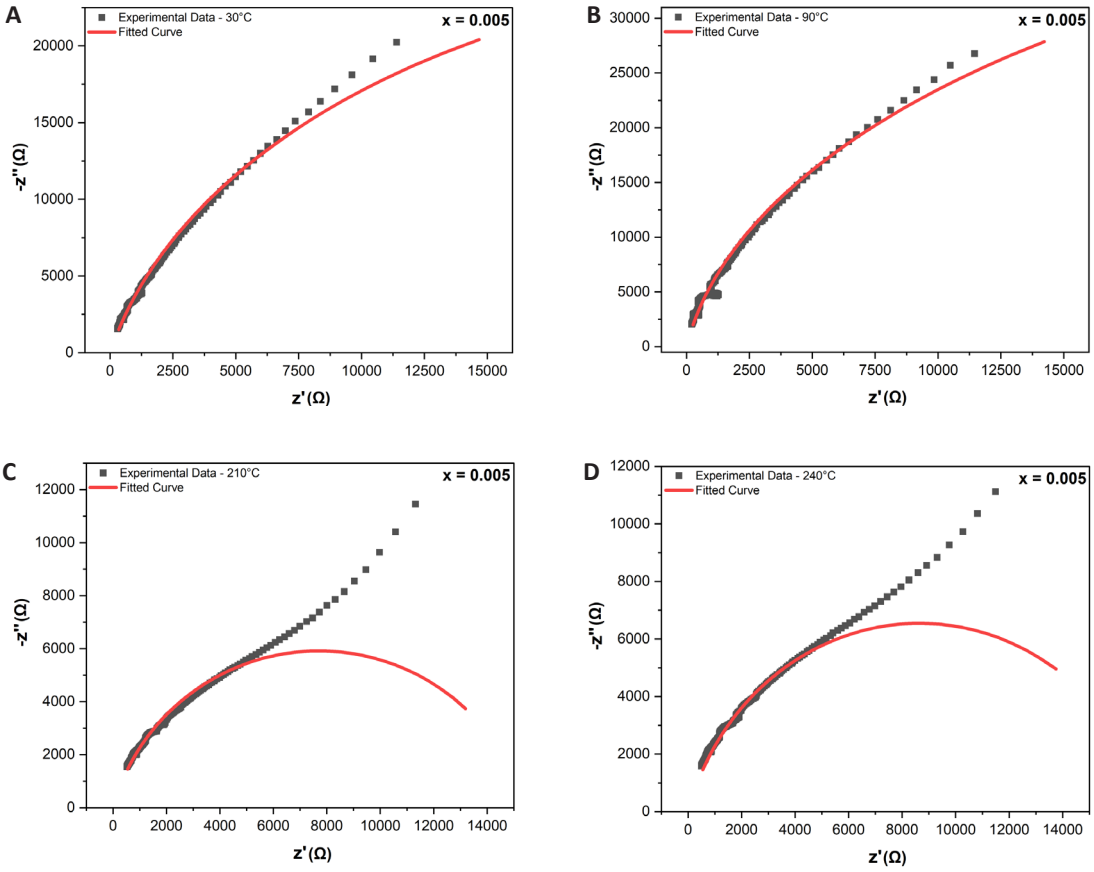


Figure 9. Nyquist Plots for Ni0.99Mg0.005Ru0.005O Nanoparticles as a Function of Frequency (0.1-8MHz) at Selected Temperatures. A: 30°C, B: 90°C, C: 210°C, D: 240°C.

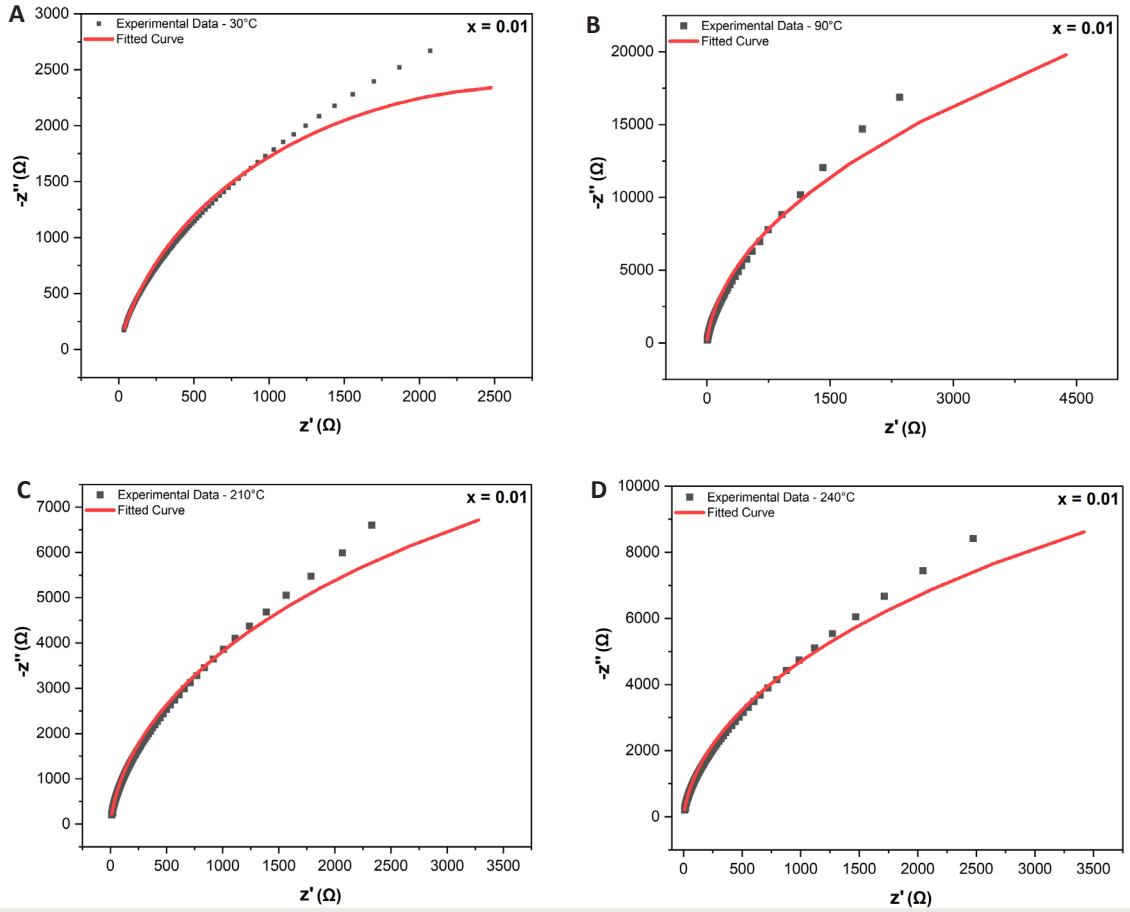


Figure 10. Nyquist Plots for $Ni_{0.98}Mg_{0.01}Ru_{0.01}O$ Nanoparticles as a Function of Frequency (0.1- 8MHz) at Selected Temperatures. A: 30°C, B: 90°C, C: 210°C, D: 240°C.

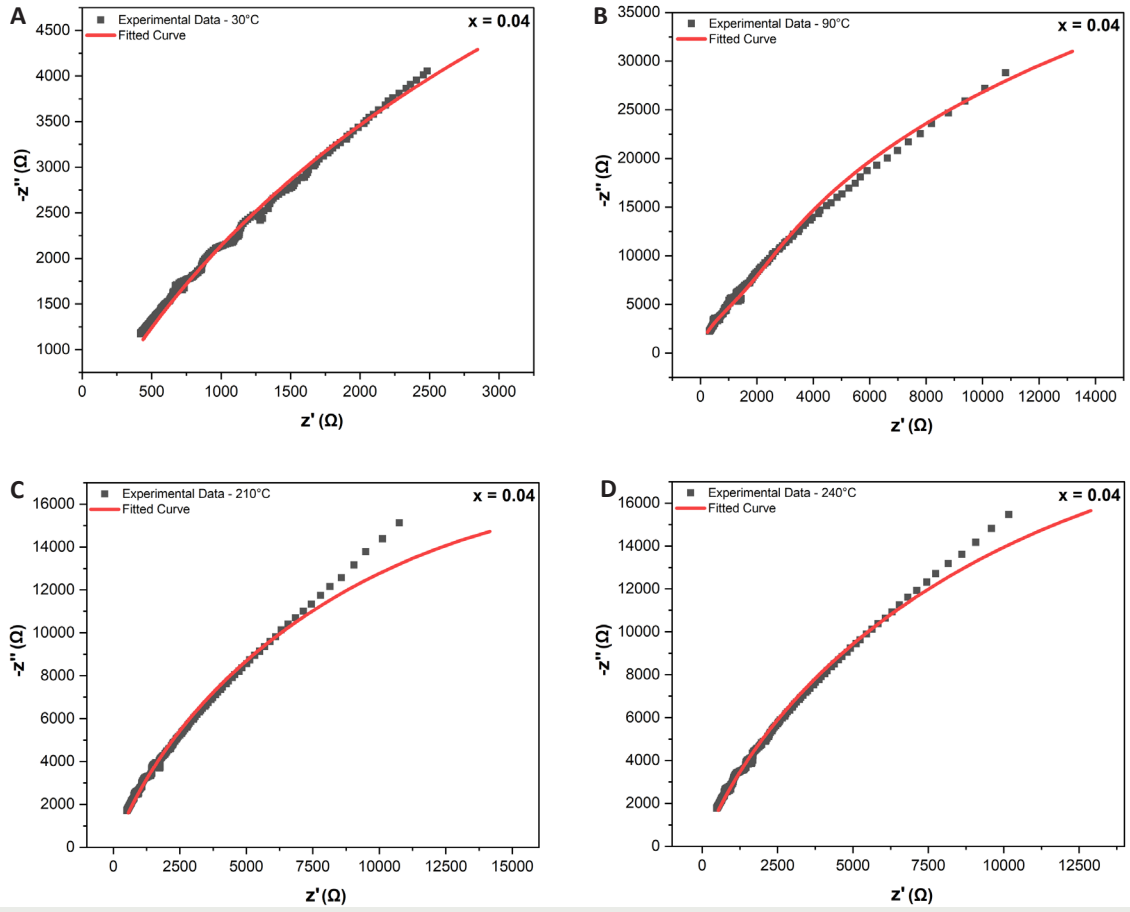


Figure 11. Nyquist Plots for $Ni_{0.92}Mg_{0.04}Ru_{0.04}O$ Nanoparticles as a Function of Frequency (0.1-8MHz) at Selected Temperatures. A: 30°C, B: 90°C, C: 210°C, D: 240°C.

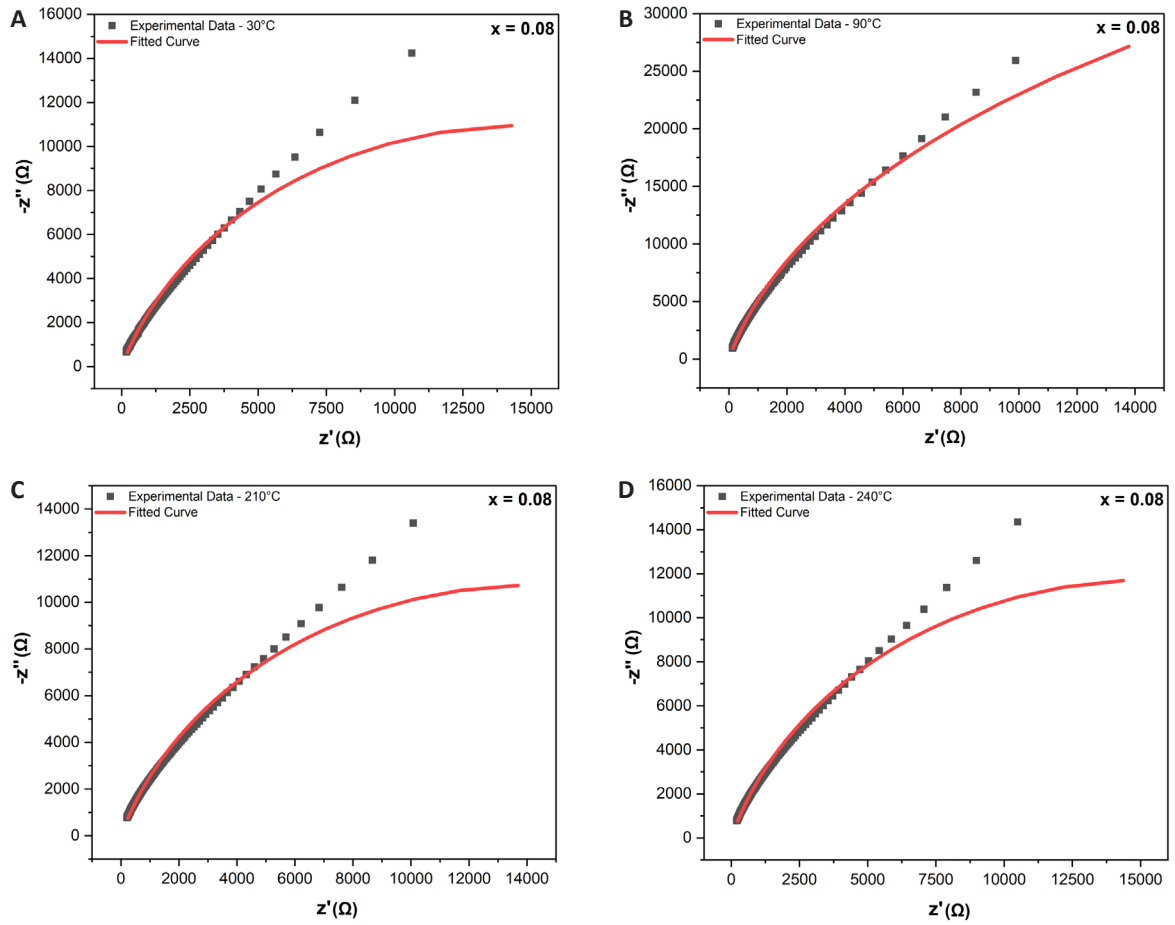


Figure 12. Nyquist plots for $Ni_{0.84}Mg_{0.08}Ru_{0.08}O$ nanoparticles as a function of frequency (0.1 8MHz) at selected temperatures. A: 30°C, B: 90°C, C: 210°C, D: 240°C.

reveal four distinct equivalent electric-circuit configurations, each corresponding to different conduction and relaxation mechanisms that are influenced by doping concentration and thermal activation.

The most common and simplest model observed was the constant phase element in parallel with a resistance (CPE // R_s) shown in Figure 13A, found in nearly all samples at 30°C and 90°C, including x=0.005, 0.01, 0.04, 0.08, and even pure NiO at 30°C. This model designates a single dominant relaxation process likely attributed to grain interior conduction with near-ideal capacitive behavior, as reflected in n1 values. By referring to Table 3, the CPE's exponent n_1 (0.75-0.99) approached unity at higher temperatures, 90°C, where n_1=(0.931, 0.989, 0.919) for x=0.005, 0.01, and 0.08, respectively, revealing thermally reduced surface heterogeneity and more ideal capacitive behaviour. Significantly, x=0.01 has n_1 remaining close to unity at high temperatures (0.972 at 210°C and 0.979 at 240°C), indicating a near-ideal capacitive response with low surface inhomogeneity and minimal involvement from multiple relaxation mechanisms. This suggests that our specific doping level at x=0.01 achieved the perfect defect ratio, where it was forming a stable microstructure from the combined co-doping from Mg^{2+} and Ru^{4+}, thus preventing the formation of charge-trapping sites or excessive mobile defects. On the other hand, x=0.005 demonstrates a significant drop in n_1 as the temperature increases (0.799 at 210°C). R_1 increased with temperature, for x=0.005, from 59.922Ω at 30°C to 87.121Ω at 90°C due to dopant-induced defect scattering, then reduced sharply at 210°C to 18.561Ω, as thermal activation dominated. Significantly, the x=0.01 sample maintained this model even at higher temperatures (210°C and 240°C), suggesting that this doping level stabilizes the electrical response and suppresses more complex mechanisms. Conversely, at higher temperatures (particularly 210°C and 240°C), samples such as x=0.005 and pure NiO at 90°C transitioned to a more complex model where (CPE // R_s) is in series with a short Warburg (W_s) element shown in Figure 13B, indicating the onset of ionic diffusion processes and additional impedance contributions from charge carrier transport limitations[55,56]. The fact that x=0.01 does not show an associated Warburg element again suggests that the doping level is inhibiting the mobility of oxygen vacancies. Therefore, the pathway was maintained as a single dominant electronic conduction, ensuring electrical stability. The comparison reveals the important role of dopant concentration, which influences defect generation, charge transport pathways, and thermally activated relaxation in (Mg, Ru) co-doped NiO nanoparticles. However, a study conducted on pure NiO nanoparticles

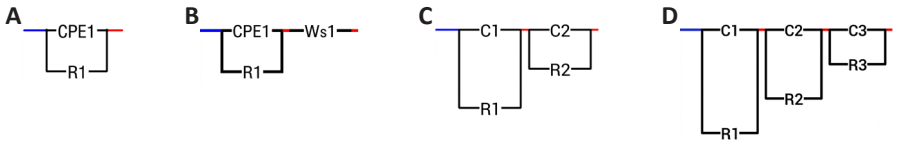


Figure 13. Equivalent Electric Circuit for the Fitted Models of $Ni_{1-2x}Mg_xRu_xO$ Nanoparticles at Selected Temperatures (30, 90, 210, and 240°C). A: x=0.005, B: x=0.01, C: x=0.04, D: x=0.08.

Table 3. Values of the Resistance (R_1), Pre-factor of the CPE (P_1), Exponent of the CPE (n_1), Warburg Short Resistance (Wsr_1), and Warburg Short Time Constant (Wsc_1) for $Ni_{1-2x}Mg_xRu_xO$ (x=0, 0.005, 0.01, 0.04, and 0.08) Nanoparticles at Selected Temperatures

x	T (°C)	R_1 (Ω)	P_1 ($\Omega^{-1}.s^{n1}$)	n_1	Wsr_1 (Ω)	Wsc_1 (s)
0	30	59875	2.1392e-11	0.90229	-	-
	90	17339	4.3125e-11	0.85945	1.0077e-13	8.4058e-14
0.005	30	59922	3.846e-11	0.87273	-	-
	90	87121	9.6608e-12	0.93196	-	-
	210	18561	1.4839e-10	0.79987	3.6711e-13	1.9508e-13
	240	19703	1.1185e-10	0.81377	1.1568e-13	1.4593e-13
0.01	30	5567.5	2.0783e-10	0.89427	-	-
	90	90012	2.9682e-11	0.98921	-	-
	210	17989	4.143e-11	0.97263	-	-
	240	26185	3.6394e-11	0.97911	-	-
	30	36724	4.9471e-10	0.75187	-	-
0.04	210	43416	1.1608e-10	0.80944	-	-
	240	48356	8.2546e-11	0.82596	-	-
	30	29590	2.858e-10	0.81144	-	-
0.08	90	92228	2.927e-11	0.91299	-	-
	210	28649	2.1129e-10	0.81909	-	-
	240	30886	1.8105e-10	0.82668	-	-

Table 4. Values of the Resistance (R_1, R_2, R_3) and the Capacitance (C_1, C_2, C_3) for Pure NiO and $Ni_{0.92}Mg_{0.04}Ru_{0.04}O$ Nanoparticles at Selected Temperatures

x	T (°C)	C_1 (F)	C_2 (F)	C_3 (F)	R_1 (Ω)	R_2 (Ω)	R_3 (Ω)
0	210	7.3662e-11	4.1586e-12	9.6048e-11	672.24	685.66	5085.9
	240	9.4629e-11	5.4766e-12	1.2088e-10	358.1	296.74	1711.8
0.04	90	3.5152e-12	7.3914e-12	-	95827	2036.3	-

prepared by the wet chemical precipitation method found an equivalent circuit composed of two parallel resistor-CPE elements in a frequency range (10^2-10^6Hz) between 30 and 130°C[57]. More structurally complex behaviors emerged in the x=0.04 sample at 90°C that required a double RC configuration shown in Figure 13C, (C_1 // R_1) in series with (C_2 // R_2), indicating two discrete relaxation processes, likely due to the interplay between grain and grain boundary conduction due to the introduction of doping which produced local distortions that became active at this intermediate temperature. Finally, the most sophisticated model shown in Figure 13D, consisting of (C_1 // R_1) – (C_2 // R_2) – (C_3 // R_3), was observed in pure NiO at 210°C and 240°C, suggesting the activation of three distinct electrical pathways involving grain interiors, grain boundaries, and interfacial or electrode effects. According to Table 4, (R_1, R_2, and R_3) drop from 672.24, 685.66, and 5085.9Ω at 210°C to 358.1, 296.74, and 1711.8Ω at 240°C, respectively, consistent with thermally lowered interfacial barriers. These results highlight the importance of doping and temperature in modulating conduction dynamics, with low-doped samples preserving simple conduction paths. However, high doping and thermal energy foster complex, multi-layered relaxation mechanisms that require increasingly complicated equivalent circuit representations.

The EIS-resolved grain-interior permittivity (ε'_{grain}) was extracted from the equivalent circuit capacitance values using the following equation:

$$\varepsilon' = C \times t / (\varepsilon_0 \times A) \quad (5)$$

Where C is the capacitance of each RC element, t=2.74mm is the pellet thickness, and A=127mm² is the pellet area.

For circuits containing multiple RC elements, the physical assignment of each element (grain interior, grain

Table 5. EIS-resolved Permittivity Components for Pure $Ni_{1-2x}Mg_xRu_xO$ (x=0, 0.005, 0.01, 0.04, and 0.08) Nanoparticles at Selected Temperatures

x	T (°C)	Circuit model	ε'grain	ε'GB / interface	ε'electrode	χ^2 ($\times10^{-3}$)
0	30	CPE//R	12.0	-	-	0.312
0	90	CPE//R	10.5	-	-	0.428
0	210	3×(RC)	10.1	179.5	234.0	0.846
0	240	3×(RC)	13.3	230.6	294.6	0.917
0.005	30	CPE//R	14.1	-	-	0.287
0.005	90	CPE//R	8.5	-	-	0.401
0.005	210	CPE//R + Ws	14.7	-	-	1.134
0.005	240	CPE//R + Ws	13.8	-	-	1.216
0.01	30	CPE//R	100.6	-	-	0.536
0.01	90	CPE//R	62.9	-	-	0.618
0.01	210	CPE//R	67.9	-	-	0.643
0.01	240	CPE//R	66.0	-	-	0.689
0.04	30	CPE//R	32.9	-	-	0.372
0.04	90	2×(RC)	18.0	8.6	-	0.758
0.04	210	CPE//R	16.0	-	-	0.481
0.04	240	CPE//R	14.7	-	-	0.509
0.08	30	CPE//R	46.1	-	-	0.394
0.08	90	CPE//R	21.0	-	-	0.522
0.08	210	CPE//R	36.2	-	-	0.601
0.08	240	CPE//R	34.9	-	-	0.648

boundary/interface, or electrode contact) was determined by ranking the characteristic frequencies ($f_c=1/(2\pi RC)$). The highest-frequency element corresponds to the grain interior, as grains are the least resistive region and therefore relax fastest. For CPE//R circuits, an effective capacitance is designated by the following equation:

$$C_{eff}=P^{1/n} \times R^{(1-n)/n} \quad (6)$$

Where P is the CPE pre-factor and n is the exponent[58], and ε' was then derived as above. The results are summarised in Table 5. For pure NiO at 210 and 240°C, the triple RC decomposition yields ε'_{grain}=10.1 and 13.3, respectively, in close agreement with the known intrinsic permittivity of NiO (ε'≈11–12)[13], confirming the validity of this decomposition. The grain boundary contribution for pure NiO is substantially inflated (ε'_{GB}=179.5 at 210°C), consistent with well-known Maxwell–Wagner space-charge accumulation at grain boundaries in polycrystalline NiO[13]. For x=0.04 at 90°C, the only temperature at which the double RC circuit separates two discrete processes, the grain interior yields ε'_{grain}=18.0 (f_c=10.6MHz), while the NiO–RuO_2 interface contributes an additional $\varepsilon'_{interface}$=8.6 (f_c=0.5MHz) directly attributable to the RuO_2 secondary phase. This quantitatively confirms that the macroscopic ε' values reported in Section 4.2 for x≥0.04 carry a significant interfacial contribution not present in the single-phase samples. For the CPE//R samples (x=0.005, 0.01, 0.04, and 0.08 at temperatures where only one process is resolved), the extracted ε' represents an integrated grain-level response combining grain interior and any unresolved interfacial effects. Critically, x=0.01 consistently yields the highest EIS-resolved ε' across all temperatures (62.9-100.6), reflecting the superior polarization efficiency of substitutional Ru fully dissolved in the NiO lattice. By contrast, the grain interior ε' for x=0.04 at 90°C is only 18.0, confirming that Ru segregation into the RuO_2 secondary phase depletes the pool of lattice-active Ru ions and reduces the intrinsic dielectric enhancement of the NiO matrix.

4 CONCLUSION

Pure NiO and $Ni_{1-2x}Mg_xRu_xO$ nanoparticles were synthesized by the co-precipitation method with different dual dopant concentrations (x=0.005, 0.01, 0.04, 0.08). The face-centered cubic structure of NiO was preserved even after introducing (Mg, Ru) dual dopants. The Rietveld refinements of the XRD patterns proved the pure form of the cubic NiO phase. However, RuO_2 secondary phase was indicated for $Ni_{0.92}Mg_{0.04}Ru_{0.04}O$ and $Ni_{0.84}Mg_{0.08}Ru_{0.08}O$ nanoparticles. $Ni_{1-2x}Mg_xRu_xO$ exhibited increasing values in the dielectric constant and AC conductivity as the temperature increased from 30°C until it peaked at around 210°C and then dropped. However, the impedance decreased with rising temperature, and tan δ revealed a more complicated temperature dependency. All samples showed sharper increases or decreases at lower frequencies than higher ones for different dielectric parameters. Nyquist plots revealed different equivalent circuit models varying with doping and temperature, signifying a complex behavior. Due to high tanδ and impedance values and temperature dependence, gas sensors may be potential applications

of pure NiO, $Ni_{0.98}Mg_{0.01}Ru_{0.01}O$, and $Ni_{0.84}Mg_{0.08}Ru_{0.08}O$ nanoparticles. However, pure and (Mg, Ru) co-doped (x=0.01) NiO nanoparticles may be suitable for energy storage devices, having high dielectric constant values and moderate AC conductivity.

Acknowledgements

Not applicable.

Conflicts of Interest

The authors declared no conflict of interest.

Author Contribution

Alkhatib A wrote the original draft, curated the data, performed the software, conducted the investigation and formal analysis, and edited the manuscript, while Bitar Z supervised the work, reviewed and edited the manuscript, conceptualized the study, and validated the findings.

Data Availability

The datasets generated during and/or analyzed during the current study are available from the corresponding author on reasonable request.

Abbreviation List

E_a, Activation energy
ESI, Electronic supplementary information
MW, Maxwell-Wagner
NiO, Nickel oxide
QMT, Quantum mechanical tunneling
SPH, Small polaron hopping
TGA, Thermogravimetric analysis
XRD, X-ray diffractometer

References

[1] Sun W, Govindarajan N, Prajapati A et al. Insights into the electrochemical oxidation and reduction of nickel oxide surfaces. *ACS Appl Mater Interfaces*, 2025; 17: 2365-2375.[DOI]

[2] Li ZH, He JX, Li JY et al. Native defect-dependent ultrafast carrier dynamics in p-type dopable wide-bandgap NiO. *J Phys Chem Lett*, 2025; 16: 175-183.[DOI]

[3] Singla S, Kalra D, Saini A et al. Influence of Mg doping on the structural and optical properties of manganese oxide (Mn_2O_3) nanoparticles. *J Phys Conf Ser*, 2023; 2663: 012007.[DOI]

[4] Aamir MF, Ali A, Nadeem K. Tuning dielectric properties in metal-doped NiO nanoparticles. *Charact Appl Nanomater*, 2025; 8: 10521.[DOI]

[5] Ahmed AAA, Alahsab EAA, Abdulwahab AM. The influence of Zn and Mg doping on the structural and optical properties of NiO nano-structures for optoelectronic applications. *Results Phys*, 2021; 22: 103938.[DOI]

[6] Abdallah AM, Awad R. Influence of Ru dopants on the structural, optical, and magnetic properties of nickel oxide nanoparticles. *Phys B Condens Matter*, 2022; 629: 413651.[DOI]

[7] Kashyap R, Poria K, JR J et al. Power generation using hydrothermally synthesized mesoporous Mg substituted NiO based on-photo catalytic hydroelectric cell. *Mater Sci Eng B*, 2024; 299: 117000.[DOI]

[8] Al Boukhari J, Bitar Z, Azab AA et al. Synthesis and physical properties of pure NiO and $Ni_{1-2x}Mg_xM_xO$ (M=Cu, Ru) nanoparticles: Role of growth temperature. *J Alloys Compd*, 2023; 969: 172500.[DOI]

[9] Patsidis AChr, Psarras GChr. Basic principles of dielectrics. In: Zha J, Dang Z, eds. High Temperature Polymeric Dielectrics. 1st ed. Wiley:Hoboken, USA, 2024: 21-55.[DOI]

[10] Padhi PS, Ajimsha RS, Rai SK et al. Process temperature-dependent interface quality and Maxwell–Wagner interfacial polarization in atomic layer deposited Al_2O_3/TiO_2 nanolaminates for energy storage applications. *Nanoscale*, 2023; 15: 8337-8355.[DOI]

[11] Siddique MN, Ahmed A, Ali T et al. Frequency dependent dielectric properties of Sr doped NiO nanostructures. *AIP Conf Proc*, 2018; 1953: 050037.[DOI]

[12] Khan I, Khan S, Khan W. Temperature-dependent dielectric and magnetic properties of Mn doped zinc oxide nanoparticles. *Mater Sci Semicond Process*, 2014; 26: 516-526.[DOI]

[13] Lin YH, Li M, Nan CW et al. Grain and grain boundary effects in high-permittivity dielectric NiO-based ceramics. *Appl Phys Lett*, 2006; 89: 032907.[DOI]

[14] Carey JJ, Legesse M, Nolan M. Low valence cation doping of bulk Cr_2O_3: charge compensation and oxygen vacancy formation. *J Phys Chem C*, 2016; 120: 19160-19174.[DOI]

[15] Flores-Ramirez R, Huanosta A, Amano E et al. Curie–Weiss behavior in polycrystalline barium titanate from AC measurements. *Ferroelectrics*, 1989; 99: 195-201.[DOI]

[16] Winkler E, Zysler RD, Mansilla MV et al. Surface spin-glass freezing in interacting core–shell NiO nanoparticles. *Nanotechnology*, 2008; 19: 185702.[DOI]

[17] Yong-Chang M, Jian-Zhu Z, Jie Z et al. Temperature- and frequency-dependent dielectric properties of $La_{1.5}Sr_{0.5}NiO_4$–δ. *Chin Phys Lett*, 2010; 27: 087701.[DOI]

[18] Slade TJ, Grovogui JA, Kuo JJ et al. Understanding the thermally activated charge transport in $NaPb_mSbQ_{m+2}$ (Q=S, Se, Te) thermoelectrics: weak dielectric screening leads to grain boundary dominated charge carrier scattering. *Energy Environ Sci*, 2020; 13: 1509-1518.[DOI]

[19] Karsthof R, Grundmann M, Anton AM et al. Polaronic interacceptor hopping transport in intrinsically doped nickel oxide. *Phys Rev B*, 2019; 99: 235201.[DOI]

[20] Petrykin V, Macounova K, Okube M et al. Analysis of local structure of $Ru_{1-x}Ni_xO_2$ electrocatalytic materials. *J Phys Conf Ser*, 2009; 190: 012166.[DOI]

[21] Lin J, Wang H, Wang C et al. Ru-modulated morphology and electronic structure of nickel organic framework bifunctional electrocatalyst for efficient overall water splitting. *Electrochim Acta*, 2023; 470: 143300.[DOI]

[22] Mao G, Yang Y, Yao Y et al. Boron and magnesium ions co-doping synergistically enhances the electrochemical performance of nickel-rich cathode materials. *Research Square*, 2023.[DOI]

[23] Gomez-Martin A, Reissig F, Frankenstein L et al. Magnesium substitution in Ni-rich NMC layered cathodes for high-energy lithium ion batteries. *Adv Energy Mater*, 2022; 12: 2270029.[DOI]

[24] Iguchi E, Akashi K. Dielectric relaxations and electrical transport due to nonadiabatic small polarons in p-type NiO doped with Li. *J Phys Soc Jpn*, 1992; 61: 3385-3393.[DOI]

[25] Chen Y, Sakata O, Yamauchi R et al. Lattice distortion and electronic structure of magnesium-doped nickel oxide epitaxial thin films. *Phys Rev B*, 2017; 95: 245301.[DOI]

[26] Zak JJ, Zuba M, Lebens-Higgins ZW et al. Irreversible anion oxidation

leads to dynamic charge compensation in the Ru-poor, Li-rich cathode $Li_2Ru_{0.3}Mn_{0.7}O_3$. *ACS Energy Lett*, 2023; 8: 722-730.[DOI]

[27] Gupta P, Maurya S, Pandey NK et al. Structural, electrical and humidity sensing properties of nano-structured nickel oxide prepared by sol–gel method. *J Mater Sci Mater Electron*, 2021; 32: 3529-3542.[DOI]

[28] Tharayil NJ, Sagar S, Raveendran R et al. Dielectric studies of nanocrystalline nickel–cobalt oxide. *Phys B Condens Matter*, 2007; 399: 1-8.[DOI]

[29] Hunnestad KA, Schultheiß J, Mathisen AC et al. Quantitative mapping of chemical defects at charged grain boundaries in a ferroelectric oxide. *Adv Mater*, 2023; 35: 2302543.[DOI]

[30] Sheena PA, Hitha H, Sreedevi A et al. Influence of finite size and surface effects on the structural, electrical and magnetic properties of nanostructured nickel oxide. *J Mater Sci Mater Electron*, 2020; 31: 5769-5778.[DOI]

[31] Usha V, Kalyanaraman S, Vettumperumal R et al. A study of frequency dependent electrical and dielectric properties of NiO nanoparticles. *Phys B Condens Matter*, 2017; 504: 63-68.[DOI]

[32] Ansari SA, Nisar A, Fatma B et al. Temperature dependence anomalous dielectric relaxation in Co doped ZnO nanoparticles. *Mater Res Bull*, 2012; 47: 4161-4168.[DOI]

[33] Hemalatha KS, Sriprakash G, Ambika Prasad MVN et al. Temperature dependent dielectric and conductivity studies of polyvinyl alcohol–ZnO nanocomposite films by impedance spectroscopy. *J Appl Phys*, 2015; 118: 154103.[DOI]

[34] Vallalperuman K, Parthibavarman M, Sathishkumar S et al. Synthesis and characterization of Co and Mn doped NiO nanoparticles. *Korean J Chem Eng*, 2014; 31: 639-643.[DOI]

[35] Węgierek P, Billewicz P. Changes in the activation energy of radiation defects in strongly defected silicon depending on the type and concentration of dopant. *Acta Phys Pol A*, 2014; 125: 1392-1396.[DOI]

[36] Dionne GF. Spin states and electronic conduction in Ni oxides. *J Appl Phys*, 1990; 67: 4561-4563.[DOI]

[37] Cheng Z, Deng W, Chen R et al. Promoted formation of catalytically active species in Ni nanoparticles by low content Ru doping for electrocatalytic oxidation of 5-hydroxymethylfurfural. *ACS Sustain Chem Eng*, 2023; 11: 13441-13450.[DOI]

[38] Biju V, Abdul Khadar M. Analysis of AC electrical properties of nanocrystalline nickel oxide. *Mater Sci Eng A*, 2001; 304-306: 814-817.[DOI]

[39] Geng ZM, Yao JS, Cheng YB et al. High-temperature phonon coherence and tunneling effect in semiconductor superlattices. *arXiv*, 2024.[DOI]

[40] Yang W, Qian H, Gan J et al. Effects of Lu and Ni substitution on thermoelectric properties of $Ca_3Co_4O_9+\delta$. *J Electron Mater*, 2016; 45: 4171-4176.[DOI]

[41] Peláiz-Barranco A, Gutiérrez-Amador MP, Huanosta A et al. Phase transitions in ferrimagnetic and ferroelectric ceramics by AC measurements. *Appl Phys Lett*, 1998; 73: 2039-2041.[DOI]

[42] Abdel Kader MM, Elzayat MY, Hammad TR et al. Dielectric permittivity, AC conductivity and phase transition in hydroxyl ammonium sulfate. *Phys Scr*, 2011; 83: 035705.[DOI]

[43] Marselin MA, Jaya NV. Structural, optical and high pressure electrical resistivity studies of pure NiO and Cu-doped NiO nanoparticles. *Int J Mod Phys B*, 2016; 30: 1650056.[DOI]

[44] Koshy J, Soosen SM, Chandran A et al. Correlated barrier hopping of CuO nanoparticles. *J Semicond*, 2015; 36: 122003.[DOI]

[45] Bolotov VV, Vishnyakov AV. Hopping mechanism of hole transport in SiO_2 at cryogenic temperatures. *Phys Status Solidi B*, 1993; 176: 157-162.[DOI]

[46] Kirpichenkov VYa, Kirpichenkova NV, Lozin OI et al. Temperature-dependent resonant tunneling in disordered quasi-one-dimensional N–I–N junctions. *Bull Russ Acad Sci Phys*, 2016; 80: 1326-1328.[DOI]

[47] Meena R, Dhaka RS. Temperature dependent conductivity, dielectric relaxation, electrical modulus and impedance spectroscopy of Ni substituted $Na_{3+2x}Zr_{2-x}Ni_xSi_2PO_{12}$. *Phys B Condens Matter*, 2024; 690: 416209.[DOI]

[48] Lazarenko MM, Zabashta YF, Alekseev OM et al. Thermally activated processes: the underlying mechanism of activated state formation. *RSC Adv*, 2024; 14: 39242-39252.[DOI]

[49] Liu P, Li Z, Cai W et al. Fabrication of cuprous oxide nanoparticles by laser ablation in PVP aqueous solution. *RSC Adv*, 2011; 1: 847-853.[DOI]

[50] Friedman F, Weichman FL, Tannhauser DS. Hall mobility in single crystals of NiO as a function of temperature and deviation from stoichiometry. *Phys Status Solidi A*, 1975; 27: 273-279.[DOI]

[51] Iwata T, Nishi Y, Kimoto T. Dominant conduction mechanism in NiO-based resistive memories. *J Appl Phys*, 2015; 117: 225701.[DOI]

[52] Blatter G, Greuter F. Carrier transport through grain boundaries in semiconductors. *Phys Rev B*, 1986; 33: 3952-3966.[DOI]

[53] Efil E, Kaymak N, Seven E et al. Frequency dependent dielectric properties of atomic layer deposition grown zinc-oxide based MIS structure. *Phys B Condens Matter*, 2019; 568: 31-35.[DOI]

[54] Dastidar PR. Space charge limited high frequency current flow in insulators in the presence of traps. *IETE J Res*, 1969; 15: 504-508.[DOI]

[55] Athanasiou V, Konkoli Z. On the efficient simulation of electrical circuits with constant phase elements: the Warburg element as a test case. *Int J Circuit Theory Appl*, 2018; 46: 1072-1090.[DOI]

[56] Orazem ME, Ülgüt B. On the proper use of a Warburg impedance. ECS Meeting Abstracts, 2024; MA2024-02: 2116.[DOI]

[57] Gokul B, Matheswaran P, Abhirami KM et al. Structural and dielectric properties of NiO nanoparticles. *J Non-Cryst Solids*, 2013; 363: 161-166.[DOI]